# Mechanics and Ion Dynamics of Disordered Solid-State Electrolytes for Batteries

Chen, Zhimin

*DOI (link to publication from Publisher):*
10.54337/aau747045616

*Publication date:*
2024

*Document Version*
Publisher's PDF, also known as Version of record

*Citation for published version (APA):*
Chen, Z. (2024). *Mechanics and Ion Dynamics of Disordered Solid-State Electrolytes for Batteries*. Aalborg University Open Publishing. https://doi.org/10.54337/aau747045616

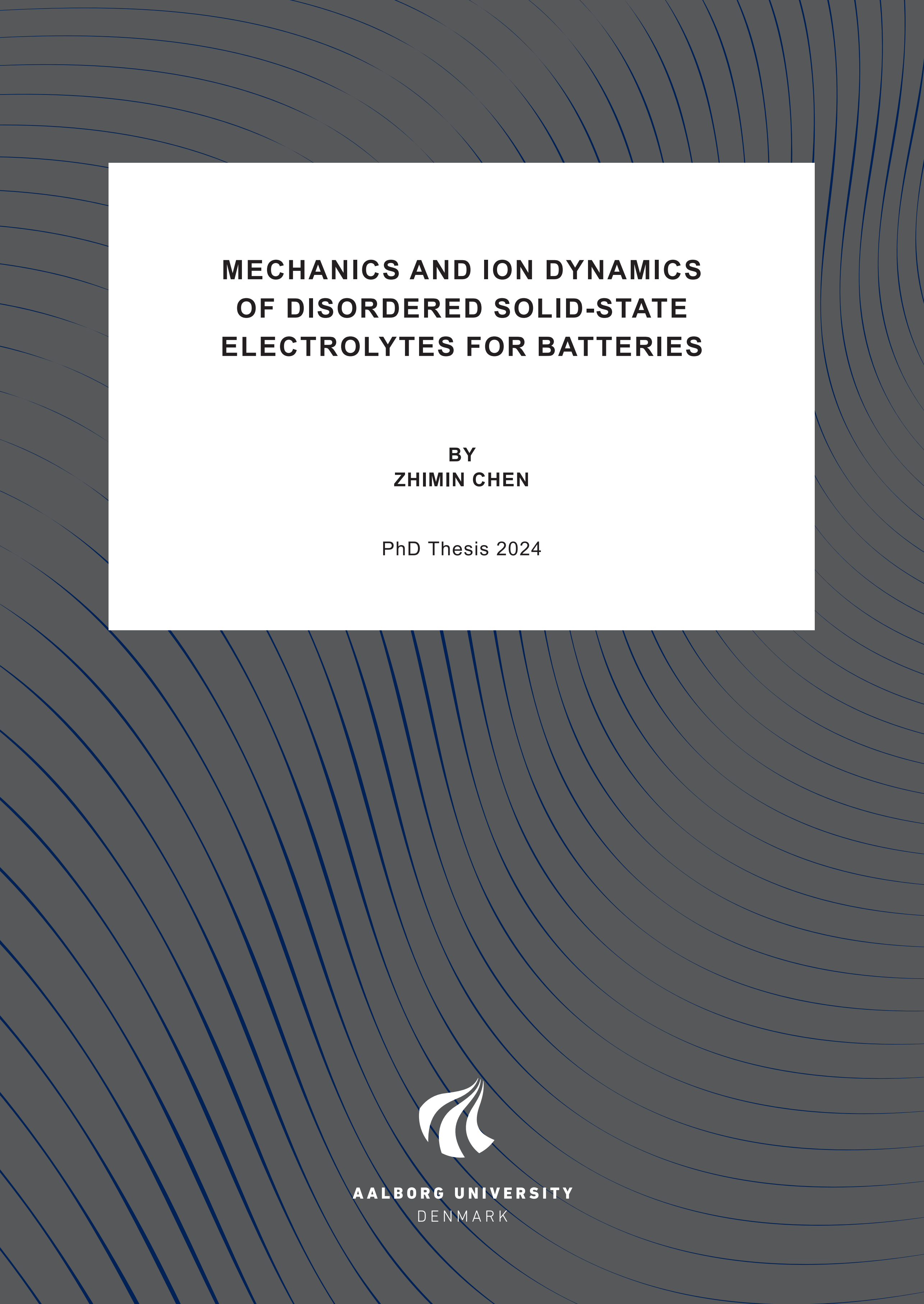

# MECHANICS AND ION DYNAMICS OF DISORDERED SOLID-STATE ELECTROLYTES FOR BATTERIES

BY
ZHIMIN CHEN

PhD Thesis 2024

AALBORG UNIVERSITY
DENMARK

# MECHANICS AND ION DYNAMICS OF DISORDERED SOLID-STATE ELECTROLYTES FOR BATTERIES

by

Zhimin Chen

AALBORG UNIVERSITY
DENMARK

PhD Thesis 2024

Submitted: July 2024

Main Supervisor: Professor Morten M. Smedskjaer
Aalborg University

Assessment: Associate Professor Mads Koustrup Jørgensen (chair)
Aalborg University, Denmark

Professor Steve Warthen Martin
Iowa State University, USA

Reader James Alexander Dawson
Newcastle University, Great Britain

PhD Series: Faculty of Engineering and Science, Aalborg University

Department: Department of Chemistry and Bioscience

ISSN: 2446-1636
ISBN: 978-87-94563-99-4

Published by:
Aalborg University Open Publishing
Kroghstræde 1-3
DK – 9220 Aalborg Øst
aauopen@aau.dk

# ENGLISH SUMMARY

Solid electrolytes are key components in battery technology, with the potential for high energy density and safety. Compared to traditional liquid electrolytes, solid electrolytes can effectively prevent leakage and combustion risks and can operate at higher voltages. Disordered or partially disordered solid electrolytes are an emerging research direction, attracting attention due to their unique structural characteristics. Theoretically, disordered structures can, at least in some cases, provide more ion migration channels, reduce ion migration resistance, and improve ionic conductivity. Additionally, disordered solid electrolytes exhibit excellent stability under high and low-temperature conditions, which is crucial for a wide range of application environments. However, disordered solid electrolytes often have issues with mechanical properties and poorly understood ion transport mechanisms, limiting their performance in practical applications and the theoretical basis for understanding ionic conductivity. The purpose of this thesis is to explore and develop the correlation between structure, mechanics, and ion dynamics in disordered solid electrolytes.

Firstly, various compositions of lithium borophosphate glass and lithium aluminum titanium phosphate (LATP) glass-ceramic electrolyte systems were experimentally studied, with atomic-scale structural changes during fracture captured by molecular dynamics simulations. Regarding its chemical, thermal, and electrochemical stability, lithium borophosphate glass is a beneficial candidate for thin-film solid batteries. We focused on the mechanical properties, as any stress between all-solid components in solid-state batteries could lead to cracks caused by stress concentration during cycling, which could result in catastrophic battery failure. Fracture toughness ($K_{Ic}$) is a defining characteristic of resistance to crack propagation, considered a significant parameter for assessing solid-state battery components. The mechanical properties of lithium borophosphate glassy electrolytes are controlled by their composition. Specifically, four-coordinated boron tends to undergo bond-switching events, i.e., changes in coordination number, which results in improved $K_{Ic}$. The fracture behavior of LATP glass-ceramics was found to be related to the crystalline phase content, with increased crystalline content enhancing the fracture energy of LATP.

Secondly, one of the most promising general candidates, lithium thiophosphate glass, is also the focus of this study. We used molecular dynamics simulations to investigate the promotion or inhibition of lithium-ion migration by different groups in lithium thiophosphate glassy electrolytes. The conclusion that $PS_4^{3-}$ promotes lithium-ion conductivity and $P_2S_6^{4-}$ inhibits it provides a theoretical basis for synthesizing lithium thiophosphate solid electrolytes with superior performance. Partial crystallization of lithium thiophosphate glass through heat treatment can increase its ionic conductivity by several orders of magnitude. By developing a machine learning potential, we could accurately simulate lithium thiophosphate electrolytes with different degrees of disorder with near-density functional theory accuracy, discovering that disorder can drive lithium ion hopping ability.

The results of this thesis deepen the understanding of the relationship between performance and structure of disordered solid electrolytes, both in terms of mechanical properties and ion migration dynamics. Specifically, four-fold coordinated boron with a tendency for bond switching plays a key role in enhancing the nanoductility of lithium borophosphate glassy electrolytes. Increasing crystalline content through heat treatment to obtain partially crystalline glass-ceramics can improve fracture energy. Our findings regarding the effect of structural groups on promoting lithium ion hopping ability and the discovery of enhanced lithium ion hopping ability by disordered structures offer novel perspectives on the principles behind ion dynamics in intricately disordered systems. This work is an important step towards understanding the mechanical basis and ion transport mechanisms of solid electrolytes with disordered structures and provides a more comprehensive understanding for designing more efficient and safer all-solid-state batteries.

# DANSK RESUME

Faststofelektrolytter er nøglekomponenter i batteriteknologi med potentiale for høj energitæthed og sikkerhed. Sammenlignet med traditionelle flydende elektrolytter kan faststofelektrolytter effektivt forhindre lækage- og forbrændingsrisici og kan operere ved højere spændinger. Uordnede eller delvist uordnede faststofelektrolytter er en fremvoksende forskningsretning, der tiltrækker opmærksomhed på grund af deres unikke strukturkarakteristika. Teoretisk set kan uordnede strukturer give flere ionmigrationskanaler, reducere ionmigrationsmodstand og markant forbedre ionledningssevnen. Derudover udviser uordnede faststofelektrolytter fremragende stabilitet ved høje og lave temperaturer, hvilket er afgørende for en bred vifte af anvendelsesmiljøer. Uordnede faststofelektrolytter har dog ofte problemer med mekaniske egenskaber og dårligt forståede iontransportmekanismer, hvilket begrænser deres ydeevne i praktiske anvendelser og den teoretiske forståelse af ionledningsevne. Formålet med denne afhandling er at udforske og udvikle sammenhængen mellem struktur og mekaniske og iondynamiske egenskaber i uordnede faststofelektrolytter.

For det første blev forskellige sammensætninger af lithiumborophosphatglas og LATP glas-keramiske elektrolytsystemer eksperimentelt undersøgt, og strukturelle ændringer på atomskalaen under brud blev fanget ved hjælp af molekylære dynamiksimuleringer. Lithiumborophosphatglas er en lovende kandidat til tyndfilmsbatterier på grund af dets termiske stabilitet, kemiske stabilitet og elektrokemiske stabilitet. Vi fokuserede på de mekaniske egenskaber af glasagtige elektrolytter, da enhver stress mellem alle faste komponenter i faststofbatterier kan føre til revner forårsaget af spændingskoncentration under cykling, hvilket kan resultere i katastrofal batterisvigt. Modstanden mod revneudbredelse er defineret ved brudsejhed ($K_{Ic}$), som betragtes som en vigtig indikator for evaluering af brudpræstationen af faststofbatterikomponenter. Det blev fundet, at brudadfærden af LATP glas-keramiker var relateret til krystallinsk faseindhold, hvor øget krystallinsk indhold forstærkede brudenergien af LATP glas-keramiske elektrolytter.

For det andet, i modsætning til de sprøde oxid-familier af faststofelektrolytter, er en af de mest lovende generelle kandidater, repræsenteret ved lithiumthiophosphat, også fokus for denne undersøgelse. Vi brugte molekylære dynamiksimuleringer til at undersøge fremme eller hæmning af lithiumionmigrationskapacitet af forskellige grupper i lithiumthiophosphatglasagtige elektrolytter. Konklusionen om, at $PS_4$ fremmer lithiumionledningsevne og $P_2S_6$ hæmmer den, giver et teoretisk grundlag for at syntetisere lithiumthiophosphat faststofelektrolytter med overlegen ydeevne. Delvis krystallisering af lithiumthiophosphatglas gennem varmebehandling kan øge dens ionledningsevne med flere størrelsesordener. Brug af mere præcise maskinlæringspotentialer gjorde det muligt for os at simulere

lithiumthiophosphatelektrolytter med forskellige grader af uorden med næsten DFT-præcision, og vi opdagede, at uorden kan drive lithiumionhoppemuligheder.

Resultaterne af denne afhandling uddyber forståelsen af sammenhængen mellem ydeevne og struktur af uordnede faststofelektrolytter, både med hensyn til mekaniske egenskaber og ionmigrationsmekanismer. Specifikt spiller firekoordineret bor med en tendens til bindingsskift en nøglerolle i at forbedre nanoduktigheden af lithiumthiophosphatglasagtige elektrolytter. Øgning af krystallinsk indhold gennem varmebehandling for at opnå delvist krystallinske glas-keramiker kan forbedre brudenergien. Vores fund om strukturelle grupper, der fremmer lithiumionhoppemuligheder, og opdagelsen af forbedrede lithiumionhoppemuligheder ved uordnede strukturer, giver nye indsigter i iondynamikmekanismerne i komplekse uordnede strukturer. Dette arbejde er et vigtigt skridt mod at forstå den mekaniske basis og iontransportmekanismerne for faststofelektrolytter med uordnede strukturer og giver en mere omfattende forståelse for at designe mere effektive og sikre fuldstændige faststofbatterier.

# ACKNOWLEDGEMENTS

This dissertation represents the culmination of several years of dedicated research and personal growth. Throughout this journey, I have received invaluable support and guidance from numerous individuals and organizations, to whom I owe a deep debt of gratitude.

First and foremost, I would like to express my heartfelt thanks to my supervisor, Professor Morten M. Smedskjaer. I still remember our first interview, applying for the China Scholarship Council together. After joining the group, you helped me adapt quickly to this wonderful team. Your expertise, unwavering support, and insightful feedback have been instrumental in shaping my research. Your encouragement and belief in my potential have driven me to strive for excellence.

Special thanks go to my colleague and friend Dr. Tao Du, postdoctoral in our group. The stimulating discussions, collaborative efforts, and camaraderie we shared have made my time here both intellectually rewarding and personally fulfilling. I am particularly grateful to Professor Yuanzheng Yue at Aalborg University, over the years, I have greatly benefited from your guidance and expertise.

I would like to thank all my collaborators whose knowledge skills and experience helped me to complete my research: Associate Professor Mathieu Bauchy, Associate Professor Lars R. Jensen, Associate Professor N. M. Anoop Krishnan, and Dr. Dmitriy Morozov.

I sincerely thank all my current and previous colleagues in the Department of Chemistry and Biology at Aalborg University. Pengfei Liu, Qi Zhang, Junwei Ding, Xuan Ge, We Fan, Xiangting Ren, Wei Xu, Yongbao Xiao, Jiajia Yan, XinXin Chen, Daming Sun, Jing Gao, Menghan Shi, Fengming Cao, Tianzhao Xu, Jingbo Ni, Yun Zhang, Xiaoyi Xu, Søren S. Sørensen, Theany To, V. N. Sudheer Ganisetti, M. Mohan Babu, Rasmus Christensen, Johan F. S. Christensen, Elsebeth J. Pedersen, Anders R. Lindbjerg, Amirhossein F. Firooz, M. Faizal Ussama, Sidsel M. Johansen, Anders K. R. Christensen, Anders M. Schade, Katrine M. Enevoldsen, Bodil A. Hansen.

I would also like to acknowledge the financial support provided by China Scholarship Council. This research would not have been possible without this funding and resources.

I extend my gratitude to the administrative and technical staff at Aalborg University for their assistance and support throughout my studies. Your dedication and efficiency have allowed me to focus on my research without unnecessary distractions.

On a personal note, I would like to thank my family for their unconditional love and support. To my parents, thank you for always believing in me and encouraging me to pursue my dreams. Your sacrifices and unwavering support have been my greatest source of strength. To my siblings, thank you for your constant encouragement and for being my pillars of support. To my girlfriend, thank you for your constant encouragement and support, your tolerance and understanding of my emotions. I love you all.

Finally, to my friends, both near and far, thank you for your understanding, patience, and encouragement throughout this journey. Your friendship has been a source of joy and motivation, and I am truly grateful for your presence in my life.

This dissertation is dedicated to all of you. Thank you for being a part of my journey.

Zhimin Chen

Aalborg University, June 12, 2024

# TABLE OF CONTENTS

# CHAPTER 1. INTRODUCTION

## 1.1. BACKGROUND AND CHALLENGES

Developing secure and efficient batteries is essential for the advancement of transportation electrification and the storage of renewable energy sources like wind and solar power[1–4]. Lithium-ion batteries (LIBs) stand out among various energy storage technologies due to their high energy and power densities, reliability, and long cycle life[5–7]. Although LIBs have significantly impacted the portable electronics market[6,8], improving battery performance, energy density, and cost-effectiveness is necessary for large-scale energy storage applications[9,10]. Additionally, due to the safety concerns and restricted energy density of conventional lithium batteries[11], t there is increasing interest in all-solid-state lithium batteries that utilize solid electrolytes.

Solid electrolytes provide several benefits like enhanced safety, increased energy density, compatibility with solid devices, and superior packaging[12]. Nonetheless, they also face issues such as lithium penetration, interface stability, and maintaining physical contact[13]. Enhancing the mechanical properties of solid electrolytes is crucial to prevent lithium dendrite growth and reduce interface stress sensitivity during electrochemical cycling. Major mechanical issues for solid-state electrolytes include deformation, crack initiation, and propagation[14]. Fracture toughness ($K_{Ic}$) is a vital measure of a solid-state battery component's resistance to crack propagation and overall fracture performance[15].

Numerous solid electrolyte materials show partial or complete disorder[15,16]. Glassy solid electrolytes, characterized by their lack of periodic structure and long-range symmetric migration paths, are disordered by nature[15]. This out-of-equilibrium state permits continuous adjustment of composition, properties, and formability[16]. Although mechanical properties significantly influence battery performance, they are often not well-characterized or understood. While some research has investigated the cracking behavior of electrode materials in lithium batteries[17] and the viscoplastic behavior of glassy sulfide electrolytes[18], there is limited data on the mechanical properties of glassy electrolyte materials. Understanding these properties in amorphous electrolytes is crucial due to the lack of crystalline defects that aid in toughening crystalline electrolytes.

Another challenge is the lack of a unified theory for ionic conduction in amorphous electrolytes[19,20]. Crystalline materials offer a well-understood platform for ionic conduction, but disordered materials lack long-range periodicity, resulting in irregular coordination sites and asymmetric long-range migration pathways. Despite considerable research efforts, a comprehensive theory for amorphous conduction has not yet been fully developed. However, ion hopping theory can still be applied if statistical treatments, such as considering the distribution of activation energies for hopping, are used. Molecular dynamics simulations are highly advantageous for studying these disordered systems, as they accurately simulate atomic-scale movements and interactions, offering deep insights into the mechanisms of ionic conduction. By leveraging the detailed dynamic descriptions provided by molecular dynamics simulations, we can gain a better understanding of ionic conduction in disordered materials. These advanced methods are essential for developing new and efficient ionic conductor materials.

## 1.2. OBJECTIVES

The purpose of this thesis is to establish relationships between the mechanical properties and structure of disordered solid electrolytes, as well as the relationship between ionic transport dynamics and structure. This will be achieved by examining a variety of disordered solid electrolyte systems to identify how their structural characteristics influence their mechanical properties and ionic transport behaviors. Special emphasis will be placed on understanding how variations in chemical composition, atomic and molecular arrangements affect these properties. Additionally, both experimental approaches and atomistic simulations will be utilized to induce and analyze structural changes with and without altering the chemical composition. By employing advanced techniques such as molecular dynamics simulations and machine learning algorithms, we aim to uncover the intricate connections between structure and function in these materials. In summary, the thesis will aim to elucidate answers to the following research questions:

- How to describe the short-range and medium-range structure of disordered solid electrolytes?

- What causes the mechanical properties and ionic migration in disordered solid electrolytes?

- What is the relationship between the mechanical properties and structure of disordered solid electrolytes?

- What is the relationship between the ionic hopping mechanisms and structure in disordered solid electrolytes?

While a comprehensive understanding of the above issues would require extensive work beyond the scope of a single thesis, this thesis aims to provide some initial steps toward answering these fundamental and insufficiently understood questions.

## 1.3. THESIS CONTENT

This thesis contains five journal papers. The papers listed below constitute the thesis content, which will be referred to by their roman numerals:

I. **Chen, Z.**, Du, T., Sørensen, S. S., Christensen, R., Zhang, Q., Jensen, L. R., Magdysyuk, O. V., Diaz-Lopez, M., Bauchy, M., Yue, Y., & Smedskjaer, M. M. (2023). Structure dependence of fracture toughness and ionic conductivity in lithium borophosphate glassy electrolytes for all- solid-state batteries. *Journal of Power Sources*, 553, 232302.

II. Du, T., **Chen, Z.**, Liu, H., Zhang, Q., Bauchy, M., Yue, Y., & Smedskjaer, M. M. (2023). Controlling factor for fracture resistance and ionic conduction in glassy lithium borophosphate electrolytes. *Materials Today Energy*, 37, 101390.

III. **Chen, Z.**, Du, T., Christensen, R., Bauchy, M., & Smedskjaer, M. M. (2023). Deciphering how anion clusters govern lithium conduction in glassy thiophosphate electrolytes through machine learning. *ACS Energy Letters*, 8(4), 1969-1975.

IV. **Chen, Z.,** Du, T., Krishnan, N. A., & Smedskjaer, M. M. (2024). Enhanced bond switching at complexion layer facilitates high fracture energy of LATP solid-state electrolytes. *Journal of Materials Chemistry A*, 12(5), 3061-3071.

V. **Chen, Z.**, Du, T., Krishnan, N. M. A., Yue, Y. Z., Smedskjaer M. M (2024). Disorder-induced enhancement of lithium-ion transport in solid-state electrolytes. arXiv preprint, 2401.05151.

# CHAPTER 2. STRUCTURE OF DISORDERED ELECTROLYTES

Crystalline electrolytes with long-range order have demonstrated excellent performance in all-solid-state batteries. Increasingly, research shows that some of the most promising solid electrolytes exhibit disordered or partially disordered structural characteristics[15]. However, the lack of long-range order in disordered structures poses challenges for establishing the relationship between performance and structure. This chapter will discuss the fundamentals of disordered structures and advanced characterization methods, providing a theoretical foundation for understanding the characteristics of disordered structures.

## 2.1. CRYSTALS AND GLASSES

Crystalline materials are characterized by a highly ordered atomic arrangement that extends over long distances, forming a repeating pattern known as a crystal lattice. This long-range periodicity gives rise to distinct and predictable properties such as well-defined melting points, mechanical strength, and electrical conductivity. The regularity of the atomic structure in crystals enables precise control over their physical properties, making them ideal for various technological applications, including semiconductors, optical devices, and structural materials. Unlike crystal, disordered materials like glass do not possess long-range periodicity. The atoms in these materials are arranged in a random, non-repeating manner, leading to unique and often complex physical properties. The absence of a regular lattice structure in disordered materials results in a lack of well-defined planes of atoms, which in turn affects their mechanical, thermal, and electrical behaviors.

Glass is one of the most common examples of a disordered solid material. Unlike crystalline solids, glass does not crystallize when it solidifies; instead, it forms an amorphous structure where the atoms are arranged randomly. Zachariasen first proposed this random network theory of glass in 1932[21]. The bonding properties in glass are the same as those in crystals, but the fundamental structural units in glass are connected in a random manner, unlike the periodic arrangement in crystalline materials. This theory has been subsequently confirmed by experimental observations (Figure 2-1), revealing the distinct differences in atomic arrangements of silica in its crystalline and disordered forms[22]. The structural disorder in glass is what enables its widespread use in applications ranging from windows and containers to optical fibers and advanced electronics.

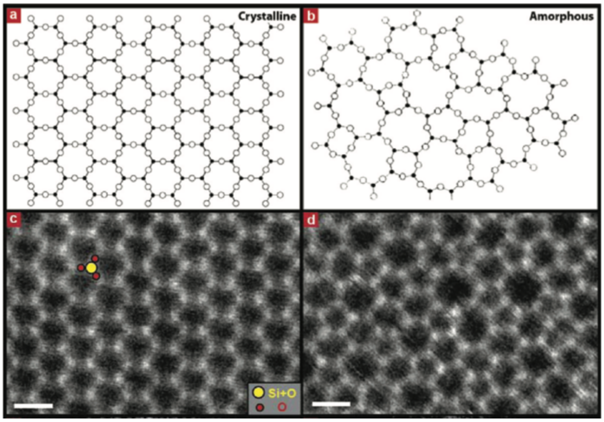

Figure 2-1 Zachariasen's models and annular dark-field scanning transmission electron microscopy images of crystal and glass silica. Figure reproduced from ref[22].

Absence of long-range order in disordered solids presents challenges in establishing clear relationships between their structure and properties. Advanced characterization techniques, such as neutron scattering and X-ray diffraction (XRD), are essential tools for probing the atomic structure of disordered materials. These techniques allow scientists to gain insights into the local and medium-range order within these materials, aiding in the development of new disordered materials with optimized properties.

## 2.2. CHARACTERIZATION OF STRUCTURAL DISORDER

Disordered materials, unlike their crystalline counterparts, lack long-range periodic order. However, they still exhibit distinct structural characteristics on different length scales, which can be categorized into short-range order (SRO) and medium-range order (MRO) (Figure 2-2). Understanding these structural features is crucial to characterize and predicting the properties of disordered electrolytes. SRO refers to the local arrangement of atoms or molecules over a few interatomic distances[23]. In this context, atoms maintain a specific coordination and bonding environment similar to that in a crystalline structure, but without extending this order beyond a few atomic distances. This means that while the immediate neighbors of any given atom are arranged in a predictable manner, this arrangement does not repeat periodically over longer distances. SRO is critical in determining the basic chemical and physical properties of the material, such as bond lengths, angles, and local density variations. MRO extends beyond the nearest neighbors, typically encompassing a range of up to a few nanometers[24–26]. It represents a level of structural organization where atoms or molecules exhibit a higher degree of correlation than in purely random arrangements but still lack the periodicity of a crystal. MRO can manifest as certain recurring motifs or clusters that provide insight into the intermediate-scale structure of the material. This order is crucial for understanding properties like diffusion, mechanical stability, and electronic behavior.

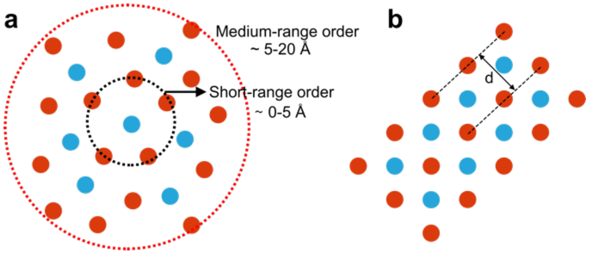

Figure 2-2 (a) Disordered material with short-range and medium-range order, where local clusters of atoms are evident without long-range periodicity. (b) Crystalline material with long-range order, where atoms are arranged in a repeating, periodic pattern.

In the subsequent sections, we will explore various characterization techniques and principles used to probe the structural features of disordered materials. Understanding these different scales of order and disorder will provide a comprehensive picture of the material's structure and properties.

### 2.2.1. LONG-RANGE ORDER STRUCTURE

XRD primarily characterizes the long-range ordered structural information of materials. As information on long-range properties of disordered materials is limited, it primarily emphasizes the differences between disordered and ordered structures, as illustrated in Figure 2-3.

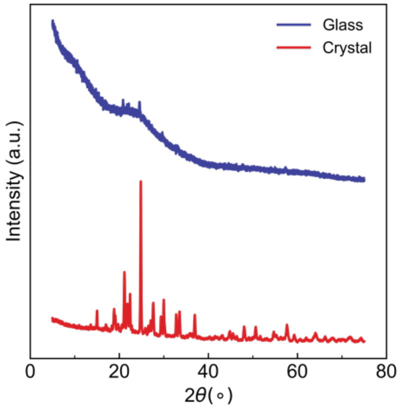

Figure 2-3 X-ray diffraction patterns of $Li_{1.3}Al_{0.3}Ti_{1.7}(PO_4)_3$ glass and crystal electrolytes. Figure adopted from Paper IV.

By measuring the diffraction angles and intensities of X-rays interacting with a crystal structure, XRD provides information about the arrangement of atoms or molecules within the crystal through Bragg's law[27]:

$$2d\sin\theta = n\lambda \tag{2.1}$$

Here, $d$ is the interplanar spacing, $\theta$ is the angle between the incident radiation and the crystal plane, and $\lambda$ is the wavelength of the incident radiation. Long-range ordered structures manifest as distinct diffraction peaks in an XRD pattern, corresponding to the interplanar spacings of the material. In disordered or amorphous materials, due to the lack of long-range order, clear diffraction peaks typically do not appear in the XRD pattern. Instead, broad and diffuse diffraction rings or scattering intensities are observed[28], reflecting the random arrangement of atoms within the material[21].

### 2.2.2. SHORT AND MEDIUM-RANGE ORDER STRUCTURE

Understanding the SRO and MRO structures of disordered solid-state electrolytes is crucial for comprehending their ion transport mechanisms and mechanical properties. Unlike crystalline materials, these electrolytes lack long-range periodicity, but they exhibit significant structural order over shorter length scales. This section delves into various techniques used to characterize these structures, emphasizing their principles and specific applications in the context of disordered solid-state electrolytes.

Short- and medium-range order structure in disordered materials can be characterized by diffraction and spectroscopic techniques. Starting from diffraction techniques, materials that exhibit from long-range order to no long-range order suppress Bragg diffraction, however, essential details are found within the diffuse scattering component[29]. Traditional diffraction analysis methods do not explicitly incorporate diffuse (elastic) scattering. Total scattering involves measuring the entire diffraction pattern, capturing both Bragg peaks and diffuse scattering, which commonly used for studying liquids and amorphous materials[30]. In scattering experiments, structural information about the sample is obtained by analyzing the changes in the wave vectors of the incident and scattered waves[29]. As shown in Figure 2-4, the wave vector of the incident wave is $k_{init}$, which propagates before hitting the sample. The central rectangle represents the sample being studied. When the incident wave interacts with the sample, scattering occurs. On the other side of the sample, the wave vector of the scattered wave $k_{final}$ differs in direction from that of the incident wave. The angle between the initial and final wave vectors of the sample is the scattering angle $2\theta$, which is the angle between the incident and scattered waves. The scattering vector $Q$ represents the difference vector between the incident and scattered waves, i.e., $Q = k_{init} - k_{final}$. This vector is directly related to the structural information of the sample[30]. The magnitude of the scattering vector is given by the formula:

$$|Q| = \frac{4\pi\sin\theta}{\lambda} \tag{2.2}$$

where $\theta$ is half of the angle between the incident and scattered waves (i.e., half of the scattering angle), and $\lambda$ is the wavelength (could be X-ray, electron, or neutron wavelength depending on the corresponding experiments) of the incident wave.

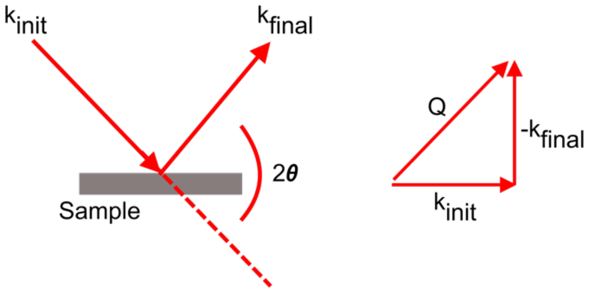

Figure 2-4 Mechanism diagram of an X-ray scattering experiment.

After omitting the complex derivation process, taking neutron scattering experiments as an example, the total neutron scattering structure factor $S(Q)$ is usually obtained after the experiment. It can be expressed as the sum of partial scattering structure factors $S_{ij}(Q)$[30]:

$$S(Q) = \frac{\sum_{i,j=1}^{n} c_i c_j b_i b_j S_{ij}(Q)}{\left(\sum_{i=1}^{n} c_i b_i\right)^2} \tag{2.3}$$

And $S_{ij}(Q)$ is directly related to the partial radial distribution function (RDF) ($g_{ij}(r)$, is defined explicitly as Eq. (2.5) through:

$$S_{ij}(Q) = 1 + \rho_0 \int_0^\infty 4\pi r^2 \left(g_{ij}(r) - 1\right) \frac{\sin(Qr)}{Qr} \mathrm{d}r \tag{2.4}$$

$$g_{ij}(r) = \frac{n_{ij}(r)}{4\pi r^2 \mathrm{d}r \rho_j} \tag{2.5}$$

where $b_i$ represents the coherent bound neutron scattering length of species $i$, averaged over its various isotopes and nuclear spin states. The fraction of species $i$ is denoted as $c_i$, $\rho_0$ is the average number density of the material, and $n_{ij}(r)$ indicates the number of particles of type $j$ within the distance range $r$ to $r+dr$ from species $i$.

After obtained $S(Q)$ from experiments, the pair distribution function (PDF) $G(r)$ can be calculated through the Fourier transform of $S(Q)$:

$$G(r) = \frac{2}{\pi} \int_0^\infty Q[S(Q) - 1] \sin(Qr) \mathrm{d}Q \tag{2.6}$$

Here, $r$ represents the real-space distance. The PDF $G(r)$ provides the probability of finding pairs of atoms separated by a distance $r$, offering detailed information about local atomic arrangements, such as bond lengths and coordination numbers.

The structure factor obtained from the experiment is not intuitive. As shown in Figure 2-5, the X-ray scattering structure factor of lithium borophosphate (LiBP, where the number of the label 38LiBP refers to the *x* value in $x\mathrm{Li_2O}$-(100-$x$)($0.5\mathrm{B_2O_3}$-$0.5\mathrm{P_2O_5}$)) glassy electrolyte, a promising candidate for thin-film solid batteries, despite changes in composition, makes it challenging to deduce any structural changes directly from the minor differences in $S(Q)$. Nevertheless, there are some methods that utilize the first sharp diffraction peak (FSDP) of $S(Q)$ as a fingerprint of the MRO structure[24,31].

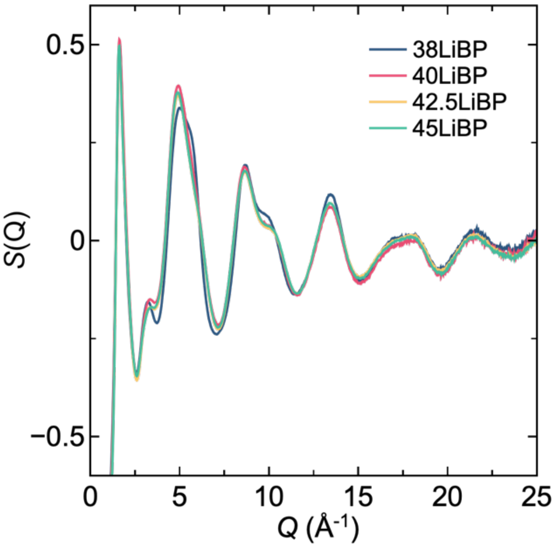

Figure 2-5 Structure factor of glasses and crystals for lithium borophosphate (LiBP) glassy electrolytes measured from X-ray total scattering experiments. The value of 38, 40, 42.5, and 45 are *x* values in $x\mathrm{Li_2O}$-(100-$x$)($0.5\mathrm{B_2O_3}$-$0.5\mathrm{P_2O_5}$). Figure reproduced for Paper I.

Neutron scattering techniques complement X-ray scattering, especially for studying materials containing light elements such as lithium. Neutron total scattering, similar to X-ray total scattering, provides insights into both long-range and local structures. The Neutron PDF is derived in a similar manner to the X-ray PDF but benefits from the isotopic sensitivity of neutrons, allowing it to distinguish between different isotopes and providing more detailed local structural information. In the disordered solid-state electrolytes, PDF analysis has been extensively used to study the local environments of lithium ions and network formers like sulfur, phosphorus, or boron in glassy electrolytes. For example, in Lithium Phosphorus Oxynitride (LiPON) glassy electrolytes, which are at the center of the search for solid-state Li metal batteries. PDF analysis (Figure 2-6) can reveal the transition from bridging nitrogen to terminal nitrogen, which appears to be directly related to the increase in ionic conductivity after the incorporation of nitrogen, as well as the trend in ionic conductivity observed in the literature[32].

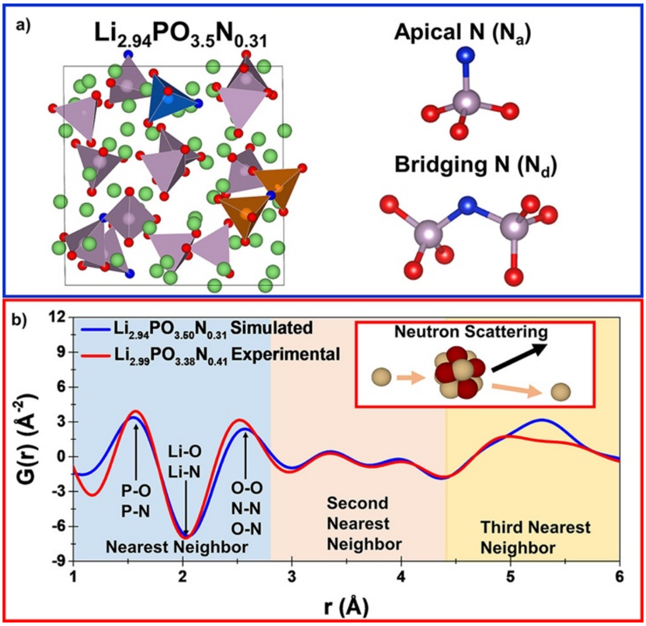

Figure 2-6 (a) Simulated $Li_{2.94}PO_{3.50}N_{0.31}$ glassy electrolytes. (b) Comparison of neutron PDF data from experiments and simulations. Figure reproduced from the Ref.[32]

Raman and Infrared (IR) spectroscopy are vibrational spectroscopy techniques that provide information about the local bonding environments[23] in disordered solid-state electrolytes. Raman spectroscopy involves inelastic scattering of monochromatic light (usually from a laser), where the energy shifts in the scattered light correspond to vibrational modes of the molecules or lattice. Raman spectra can reveal information about bond strengths, coordination environments, and the presence of specific structural units[33]. Infrared (IR) spectroscopy measures the absorption of IR radiation by the sample. The absorption frequencies correspond to vibrational transitions of the molecules. IR spectra provide complementary information to Raman spectra and can help identify different functional groups and bonding environments. In disordered solid-state electrolytes, Raman and IR spectroscopy are used to study the local structures of the glassy or amorphous network[23]. For example, in phosphate-based solid electrolytes, Raman and IR spectra can identify different phosphate units (such as $Q^0$, $Q^1$, $Q^2$ species) and their connectivity[23], which is essential to comprehending how the structure of the glass network affects ionic conductivity. Similarly, in sulfide-based electrolytes, these techniques can provide insights into the local bonding environments of sulfur and its interactions with other network formers and modifiers[34–37].

## 2.3. MODELING OF DISORDERED ELECTROLYTES

Experimental characterization of disordered structures has successfully provided real structural features of various materials, but the cost is high. Models can be validated against experimental data and serve as important predictive tools, allowing observation of characteristics from atomic scale that are sometimes inaccessible through experiments alone. By providing fundamental electronic and structural insights, Density Functional Theory (DFT) and DFT-based *ab initio* molecular dynamics (AIMD) simulations can precisely reproduce the structural disorder and dynamics of electrolytes. However, DFT-based simulations are expensive, and large-scale simulations are necessary in certain cases, such as fracture simulations and long-timescale dynamic properties. Therefore, molecular dynamics (MD) simulations based on classical mechanics, while sacrificing some accuracy, allow for efficient large-scale simulations. Recently, the emergence of machine learning potentials, which are trained on the results of DFT-based simulations, has led to the development of potentials that can be accelerated in classical MD simulation software[38]. These potentials improve the accuracy of atomic interactions in simulations while also enhancing computational efficiency, gradually becoming one of the primary methods for simulating disordered solid electrolytes[39]. The fundamental of these modeling techniques will be introduced in this section.

### 2.3.1. DFT-BASED SIMULATIONS

A quantum mechanical method called density functional theory (DFT) is used to analyze the electrical structure of many-body systems. The foundational concept of DFT is that the ground-state properties of a many-electron system can be determined by its electron density $\rho(\mathbf{r})$, rather than its many-body wavefunction $\Psi(\mathbf{r}_1,\mathbf{r}_2,\ldots,\mathbf{r}_N)$. This simplifies the problem significantly, as dealing with the electron density is computationally more feasible than dealing with the full wavefunction. Having established the basic principle of using electron density, it is essential to delve deeper into the theoretical underpinnings that justify this approach. This leads us to the Hohenberg-Kohn theorems[40], which form the cornerstone of DFT.

1. First Theorem: The ground-state electron density uniquely determines the external potential $V_{ext}(\mathbf{r})$, and consequently, all properties of the system.
2. Second Theorem: There exists a universal functional $E[\rho]$ of the electron density that achieves its minimum value at the true ground-state density $\rho_0(\mathbf{r})$, giving the ground-state energy of the system.

While these theorems provide the theoretical foundation, practical application of DFT requires a method to calculate the electron density. To make DFT practical, Kohn and Sham introduced a set of single-particle equations[41]:

$$\left(-\frac{\hbar^2}{2m}\nabla^2 + V_{eff}(\mathbf{r})\right)\psi_i(\mathbf{r}) = \epsilon_i\psi_i(\mathbf{r}) \tag{2.7}$$

where $V_{eff}(\mathbf{r})$ is the effective potential comprising the external potential, Hartree potential, and exchange-correlation potential. The electron density is expressed as:

$$\rho(\mathbf{r}) = \sum_i |\psi_i(\mathbf{r})|^2 \tag{2.8}$$

The effectiveness of the Kohn-Sham approach depends significantly on the choice of the exchange-correlation functional. The exchange-correlation functional $E_{xc}[\rho]$ is crucial for the accuracy of DFT calculations. Common approximations include Local Density Approximation (LDA, assumes $E_{xc}$ depends only on the local density.)[42], Generalized Gradient Approximation (GGA, incorporates the gradient of the density)[43], and Hybrid Functionals (combine a fraction of exact exchange from Hartree-Fock theory[44] with GGA).

DFT itself does not directly generate disordered electrolytes, but it can be used to optimize and analyze them. When generating disordered structures, other methods are typically combined, such as MD or Monte Carlo, followed by further optimization and electronic structure calculations using DFT. *Ab initio* MD (AIMD) integrates DFT with MD, calculating forces on-the-fly from electronic structure calculations. AIMD can model a system at high temperatures and generate disordered structures through rapid cooling. For example, by melting a crystalline structure and then rapidly quenching it to room temperature, a disordered structure is obtained. However, DFT-based simulations are generally accurate but computationally expensive as DFT involves solving for each electronic state, with the complexity increasing as the number of electrons in the system increases.

### 2.3.2. MD-SIMULATIONS BASED ON CLASSICAL FORCE FIELDS

Molecular dynamics (MD) simulations model the physical movements of atoms and molecules over time by solving Newton's equations of motion. In classical MD, atoms are treated as classical particles. The forces between them are derived from empirical potentials. The accuracy of MD simulations depends heavily on the choice of force fields and potential functions used to describe interatomic interactions. Start from Buckingham potential[45], one of the most used classical potential functions, the interactions between atoms can be expressed as follow:

$$\phi(r_{ij}) = A_{ij}e^{-B_{ij}r_{ij}} - \frac{C_{ij}}{r_{ij}^6} \tag{2.9}$$

where $A_{ij}$, $B_{ij}$, and $C_{ij}$ are constants, and the two terms on the right constitute electronic repulsive and attractive forces. For disordered electrolytes, the potential functions must accurately represent both the short-range interactions (such as covalent and ionic bonds) and long-range interactions (such as van der Waals forces and electrostatic interactions). Thus, Coulombic interactions $\frac{1}{4\pi\epsilon_0}\frac{q_i q_j}{r_{ij}}$ also need to be considered, where $q$ is the magnitude of the charge and $\epsilon_0$ is the dielectric constant. Ultimately, the interactions between atoms can be represented by the following function.

$$U_{ij} = \frac{1}{4\pi\epsilon_0}\frac{q_i q_j}{r_{ij}} + A_{ij}\exp\left(-\frac{r_{ij}}{\rho_{ij}}\right) - \frac{C_{ij}}{r_{ij}^6} \tag{2.10}$$

For disordered solid electrolytes, ion polarization plays an important role in the simulation of defects and surfaces, as well as in the calculation of properties such as the dielectric constant. In the case of $Li_{1.3}Al_{0.3}Ti_{1.7}(PO_4)_3$ electrolytes, polarization of the multi-ionic phosphate tetrahedra can be simulated by representing oxide anions using a core-shell model. In this model, an oxide anion is composed of a core particle and a shell particle corresponding to the outer electron shell[46]. The charges of the two pseudo-particles add up to the effective charge of the oxygen ion, and the particles are connected by a harmonic spring, as illustrated below.

$$U_{\mathrm{cs}} = k \cdot r_{\mathrm{cs}}^2 \tag{2.11}$$

where $r_{cs}$ is the core-shell distance and $k$ the corresponding force constant.

Despite the progress made in MD simulations of disordered materials like glasses, several challenges remain to be addressed. One of the primary challenges is the development of empirical potentials[47]. Key inputs for MD simulations are potentials that are dependable, transportable, and efficient. Despite the fact that numerous silicate potentials have been created for silicate electrolytes, the potentials for other glass formers particularly those that contain borate remain comparatively inaccurate[47]. Another challenge is the accuracy in describing interatomic interactions. The performance of disordered electrolytes largely depends on their structure. Therefore, although MD simulations based on empirical potentials excel in computational efficiency and allow the study of systems consisting of thousands of atoms, the quality of MD simulations is limited by the accuracy of the underlying empirical potentials. In principle, the most accurate way to obtain interatomic forces or potentials is to solve the Schrödinger equation, which describes the physical laws behind most chemical phenomena and processes[48]. Hence, the development of machine learning potentials is bridging the gap between the accuracy of *ab initio* methods (DFT-based) and the efficiency of empirical potentials[39].

Using patterns or structures in the data, machine learning techniques seek to understand the functional link between inputs (chemical descriptors) and outputs (properties). A taught learning machine should ideally represent the practical “rules” of quantum physics. In practice, machine learning models can take shortcuts and do not need to solve any equations that follow the physical laws governing structure-property relationships.

## 2.4. SUMMARY

Understanding the structural characteristics of disordered materials, such as glass, is crucial for advancing their applications in various fields. In this chapter, we began with an overview of structural disorder, discussing its various manifestations and the importance of understanding these structures in the context of electrolyte materials. We then delved into the methods used to characterize structural disorder, distinguishing between long-range order structures and short- and medium-range order structures. The chapter also covered the modeling techniques used to study disordered electrolytes, provided a comprehensive look at the structural intricacies of disordered electrolytes and the methodologies used to investigate them, laying the groundwork for understanding their properties and behavior in subsequent chapters.

# CHAPTER 3. FUNDAMENTALS OF MECHANICS AND ION DYNAMICS

The mechanical characteristics of the solid electrolyte can influence the battery's microstructural changes and, as a result, its overall performance. Notably, issues such as loss of contact, fracture, and uneven electrodeposition can have disastrous effects, all of which are contingent on how the solid electrolyte matrix responds to generated stresses. Despite this, the connection between the mechanical properties of solid electrolytes and the functioning of solid-state batteries remains inadequately understood. In addition to this, for disordered solid electrolytes, the lack of long-range ordered structures creates difficulties in deciphering their ion migration mechanisms. In this chapter, we will introduce the mechanical basis of disordered solid electrolytes and the basis of ion dynamics.

## 3.1. MECHANICS

### 3.1.1. BASIS OF MECHANICS

The response of solids to external forces typically progresses through elastic and plastic deformation to fracture[49]. Elastic deformation involves reversible shape changes once the external load is removed. The extent of elastic deformation is determined by yield strength and the elastic strain limit, marking the maximum elastic stress and strain (Figure 3-1). Modulus refers to the stress required to produce a unit strain, and stiffness, which also involves force and deformation, represents a similar concept. The modulus is an intrinsic property, unaffected by the solid's shape and size, and is calculable from the linear elastic portion of the stress-strain curve (Figure 3-1). Stiffness, however, depends on both the material's properties and the solid's dimensions. Different types of moduli apply to different loading scenarios: the bulk modulus ($K$) for uniform pressure, Young's modulus ($E$) for uniaxial compression or tension, and the shear modulus ($G$) for shear forces. For two homogeneous isotropic linear elastic materials with identical Poisson's ratios, these moduli will have consistent relative magnitudes[49]. In materials science, hardness indicates resistance to local plastic deformation from mechanical indentation or wear. The solid enters the plastic deformation phase where strain becomes irreversible upon removal of the external force when stress exceeds the yield strength[49]. Ultimate strength is the highest force a material can withstand before failing. The peak stress during compression or tensile testing before to fracture is referred to as the ultimate compressive strength and ultimate tensile strength. The maximum strain before fracture is termed fracture strain, or ductility. Ductile materials exhibit significant deformability, encompassing both elastic and plastic deformation, whereas brittle materials fracture quickly after yielding, showing minimal plastic deformation capacity (Figure 3-1). The area under the stress-strain curve indicates deformation energy: resilience within the elastic region and toughness before fracture. However, fracture toughness specifically describes the ability to resist crack growth under applied stress.

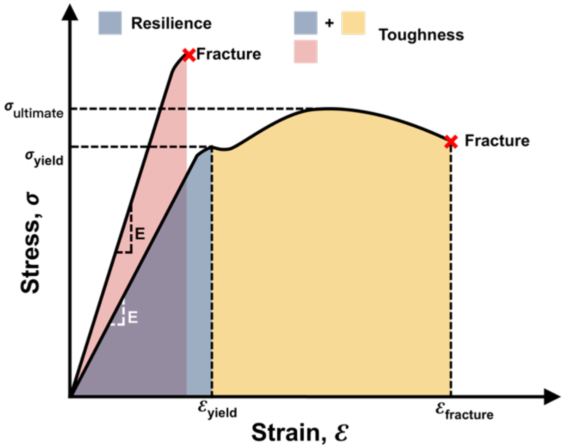

Figure 3-1 Basic mechanical properties with a typical stress-strain curve for ductile and brittle materials.

### 3.1.2. PLASTIC DEFORMATION

Disordered solid electrolytes, represented by glass, usually exhibit brittleness. The stress generated by electrochemical reactions in electrodes is referred to as electrochemical strain or electrochemical shock. The electrode material experiences periodic expansion and contraction upon the reversible insertion of mobile ions[15]. This phenomenon generates local stress, which can influence the solid electrolyte, causing the initiation and growth of cracks (Figure 3-2). The *E* and *G* are frequently used to describe how materials deform under stress, particularly during electrochemical shock. Materials with low elasticity modulus, such as sulfides, are considered ideal candidates for solid electrolytes due to their excellent capability to endure the stress exerted by electrodes during reversible ion intercalation. However, these soft materials, like lithium thiophosphate glasses, have been found to be brittle and susceptible to fracture under stress[50].

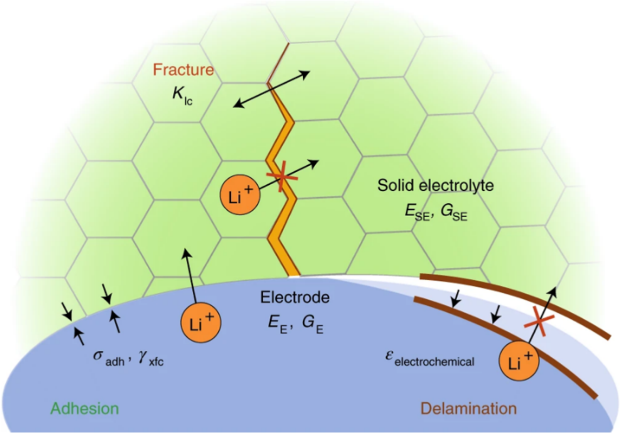

Figure 3-2 The mechanical response of solid electrolyte and electrode to strain during cycling. Figure reproduced from ref[15].

The goal of all-solid-state battery engineering is to select a combination of materials that can reversibly deform within the battery and limit stress to avoid fracture. In metallic lithium, stress accumulation can be effectively limited by diffusion flow or dislocation slip. However, crystalline electrolytes like ceramics cannot activate slip systems at room temperature, making them prone to fracture. To address this issue, introducing crystal defects intentionally during the processing stage can enhance the toughness of the materials. Using this method, material toughening is accomplished by shifting pre-existing dislocations rather than creating new ones. In order to ensure that there are enough dislocations in the limited volume surrounding the crack tip, it is necessary to purposefully introduce a high density of dislocations into the material. The effectiveness of this method has been demonstrated in titanium dioxide ($TiO_2$) through flash sintering, which introduces stacking faults and dislocations[51]. This material can undergo up to 10% deformation under compression without fracturing, and local strain slip bands similar to those in metal deformation have been observed. Recent studies also indicate the possibility of introducing dislocations and enhancing ductility in $Li_7La_3Zr_2O_{12}$ (LLZO) solid electrolyte materials[52].

Typically, glass is produced through melt casting, where the supercooled liquid creates a network that facilitates the movement of lithium ions[53]. Amorphous materials can also be generated through methods such as sputter deposition, plasma torch condensation, high-energy milling, and other rapid quenching techniques. Because these materials lack a structured framework of bonded glass formers, they are capable of incorporating higher lithium content. The primary components include oxides, sulfides, and various mixed components. While these materials are brittle on a macroscopic scale, localized densification and shear flow can reduce stress without causing fracture, which is crucial for the behavior at the lithium interface[53]. The performance of these processes varies with composition and mechanical properties, with the modulus-to-hardness ratio and Poisson's ratio being the most influential factors. An example of a disordered solid electrolyte with high fracture resistance is LiPON. Although studies on the mechanics of amorphous LiPON are limited[54], existing research indicates that when prepared as a thin film, the material is robust. The modulus-to-hardness ratio, obtained through nanoindentation measurements, is approximately 23, which is higher than that of typical oxide glasses (modulus-to-hardness = 10 to 13), indicating that LiPON possesses a degree of ductility[54]. Further research has revealed that LiPON can densify and deform under shear, thereby reducing stress intensity.

### 3.1.3. FRACTURE

If stress cannot be relieved through the lithium metal, it may need to be relieved through the solid-state electrolyte. In crystalline materials, the fracture tip typically acts as a source of dislocations that can facilitate plastic deformation to lower stress. On the other hand, dislocation nucleation in ionic crystals (i.e., cathode materials and ceramic electrolytes) needs to overcome large energy barriers. Because of this, even at extremely tiny length scales, ionic compounds are intrinsically fragile, even if their cohesive energy is higher than that of metals. Fracture resistance is correlated with ductility and measured by fracture toughness, which is a function of the critical stress needed for an existing crack to propagate. Fracture toughness is becoming a key factor in the performance of solid-state batteries. Unlike the elastic modulus, fracture toughness largely depends on microstructural parameters such as densification, grain size, impurities, and the presence of pre-existing cracks and porosity. Although the performance of solid-state batteries relies on their mechanical properties, characterizing these properties in solid electrolyte materials is relatively uncommon. Fracture in materials can generally be categorized into three basic modes based on the displacement of the crack surfaces, as shown in Figure 3-3. Among these modes, the first mode is by far the most relevant to the propagation of cracks in brittle solids. Therefore, we will only discuss the fracture toughness under pure Mode I loading, denoted as critical stress intensity factor $K_{Ic}$.

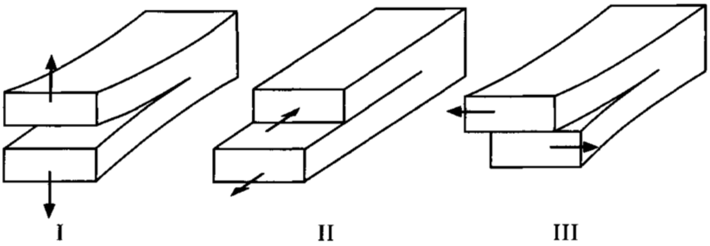

Figure 3-3 The three modes of fracture: I, opening mode; II, sliding mode; III, tearing mode. Figure reproduced from ref[55].

However, measuring this property in brittle materials, particularly glasses, is quite challenging. External factors such as temperature, chemical environment, or even light can influence the material's behavior and, consequently, the property being measured. The single-edge precracked beam (SEPB) method appears to be more appropriate for brittle materials. Beams are subjected to loading through either a three-point or four-point bending setup. $K_{Ic}$ can be calculated from the failure load using the following equation using peak load ($P_{max}$):

$$K_{\mathrm{Ic}} = \frac{P_{max}}{B\sqrt{W}} Y^* \tag{3.1}$$

where $B$ and $W$ represent the beam's width and thickness, respectively. $Y^*$ is a geometrical factor dependent on the ratio $a/W$, with $a$ being the crack length. The ASTM standard and adopted version[56,57] provide detailed experimental guidelines. Additionally, Paper I presents the detailed experimental procedures for measuring the fracture toughness of lithium borophosphate glass electrolytes. In brief, a pre-crack extending to half the sample width is first generated. The sample is then fractured using a three-point bending test, and the maximum load is recorded. The value of $Y^*$ is obtained by examining the fracture surface (Figure 3-4) and using Eqs. (3.2) and (3.3).

$$Y^* = \frac{3}{2}\frac{S}{W}\frac{\alpha^{1/2}}{(1-\alpha)^{3/2}} f(\alpha) \tag{3.2}$$

$$f(\alpha) = [1.99 - (\alpha - \alpha^2)(2.15 - 3.93\alpha + 2.7\alpha^2)]/(1 + 2\alpha) \tag{3.3}$$

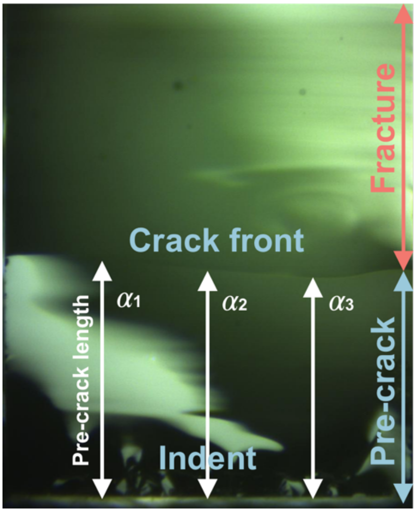

Figure 3-4 An example of a post-fractured SEPB specimen utilized in calculating fracture toughness ($K_{Ic}$). Figure reproduced for Paper I.

For various ionic and covalent materials, the fracture toughness is closely related to their composition for disordered solid electrolytes (Paper I) and appears to be closely associated with the Pugh's ratio and the volume per atom[58]. However, even for relatively tough ionic crystals (e.g., cubic spinel $MgAl_2O_4$), the fracture toughness is capped at around ~2 MPa·$m^{0.5}$, indicating that such materials can easily fracture if sufficient stress is present within initial defects. Therefore, a deeper step in the fracture structure relationship needs to be explored to discover how to avoid rapid propagation of the fracture.

## 3.2. ION DYNAMICS

Solid-state electrolytes have a very different ion conduction mechanism than liquid electrolytes. Whereas ions in solid-state electrolytes either diffuse along favored paths in crystals[15] or migrate across a disordered structural environment[[59], ions in liquid electrolytes move through the liquid medium, separated from the transport of electrons[19]. Comprehending the complexities of ionic transport in solid- state electrolytes is necessary to enhance battery performance. In crystalline solid electrolytes, ion conduction methods include tunneling, vacancy-assisted migration, and interstitial diffusion[15]. Start from crystalline solid electrolytes, ions move through a lattice by hopping from one site to another. This process is driven by thermal energy and is influenced by the crystal structure, defect concentrations, and the interactions between ions and the lattice. The ion hopping mechanism can be visualized as ions moving through a potential energy landscape. Each site in the crystal lattice corresponds to a local minimum in potential energy. The energy barriers between these sites are known as activation energies ($\Delta E$), and they must be overcome for an ion to hop from one site to another[59]. The rate of ion hopping can be described by the Arrhenius equation, which relates the hopping rate to temperature and activation energy:

$$\Gamma = \Gamma_0 \exp\left(-\frac{\Delta E}{k_B T}\right) \tag{3.4}$$

where $\Gamma$ is the hopping rate. $\Gamma_0$ is the pre-exponential factor, representing the attempt frequency. $\Delta E$ is the activation energy. $k_B$ is the Boltzmann constant. $T$ is the absolute temperature. Eq. (3.4) indicates that higher temperatures increase the ion hopping rate by providing more thermal energy to overcome the activation barriers.

Ionic conductivity ($\sigma$) in a crystalline solid is a measure of how easily ions can move through the material. It is related to the ion hopping rate and the concentration of mobile ions. The ionic conductivity can be expressed as:

$$\sigma = ne\mu \tag{3.5}$$

where $n$ is the number density of mobile ions, $e$ is the charge of the ion, $\mu$ is the mobility of the ions. The mobility ($\mu$) of ions is related to their diffusion coefficient ($D$) through the Einstein relation:

$$\mu = \frac{eD}{k_B T} \tag{3.6}$$

The diffusion coefficient $D$ can be described by the Nernst-Einstein equation:

$$D = \frac{\Gamma a^2}{6} \tag{3.7}$$

where $a$ is the distance between adjacent lattice sites. Combining these equations, the ionic conductivity can be rewritten as:

$$\sigma = ne^2 \frac{a^2 \Gamma}{6 k_B T} \tag{3.8}$$

Eq. (3.8) shows that ionic conductivity depends on the ion concentration, the square of the distance between lattice sites, the hopping rate, and the temperature. Diffusion coefficients $D$ can typically be obtained from NMR spectroscopy and MD simulations and thus to calculate ionic conductivity.

In crystals, cation vacancies or interstitials are considered mobile charged species. There are three main migration mechanisms around vacancies and interstitials: vacancy diffusion, where an ion migrates to an adjacent vacancy; direct interstitial mechanism between partially occupied sites; and the coordinated or correlated interstitial (knock-on) mechanism, where the migrating interstitial ion displaces an adjacent lattice ion to a neighboring site[15]. Combining the definition of activation energy $\Delta E$, which includes the energy required to form mobile defects ($\Delta E_f$) and the energy barrier for their migration ($\Delta E_m$)[15], increasing the concentration of defects in crystals and lowering $\Delta E_f$ also contributes to the reduction of $\Delta E$, thereby enhancing the hopping rate $\Gamma$ as seen from Eq. (3.4). For example, in $Na_3PS_4$, doping $Si^{4+}$ at the $P^{5+}$ site generates $Na^+$ interstitials[60], while doping $Cl^-$ at the $S^{2-}$ site creates $Na^+$ vacancies[61]. These modifications can ultimately lead to an increase in ionic conductivity.

Because the energy landscape in disordered or glassy solid electrolytes is naturally uneven, the mechanisms for ion conduction in these materials are still unknown[15,19,20] [59]. However, some aspects of hopping theory can still be applied; however, statistical processing is needed, for example, activation energy distributions for hopping should be taken into account instead of discrete distributions. Atomic configurations and diffusion channels in amorphous substances can be immediately revealed by using reverse Monte Carlo methods in conjunction with PDF analysis of total scattering data[62,63]. However, it is difficult to precisely predict and control ion routes due to the absence of a well-defined crystal structure. Furthermore, the comprehension of ion conduction in these materials is further complicated by the existence of flaws and disorder-induced structural heterogeneity.

## 3.3. SUMMARY

In this chapter, we present the mechanical and ionic dynamics fundamentals of disordered solid electrolytes. Understanding the basic mechanisms of elastic or plastic deformation and even fracture caused by internal stresses generated during electrochemical cycling is crucial for constructing crack-free solid electrolytes. We also introduce the ionic mechanisms in both ordered crystals and disordered solids. While the ordered solid electrolytes have well-established theoretical foundations, the hopping mechanisms, such as vacancies and defects, are no longer applicable in disordered structures. Moreover, the system size required for statistical analysis is relatively large, making it challenging to probe atomic-scale ionic dynamics through AIMD. To better understand these migration mechanisms, faster and more accurate simulation techniques may be necessary. The introduction of machine learning to identify local soft sites hidden within disordered structures can also help bridge this gap.

# CHAPTER 4. STRUCTURE AND MECHANICS RELATIONS

Deformation and cracking under stress in disordered electrolytes can cause performance degradation and even catastrophic battery failure. However, in all-solid-state batteries, there is a significant lack of understanding regarding the mechanical properties of disordered solid electrolytes. This chapter explores the connection between structure and mechanical properties, ranging from the experimental characterization of properties like modulus and fracture toughness to the examination of fracture mechanisms at the atomic scale. These investigations provide new insights into the mechanical behavior of disordered solid electrolytes.

## 4.1. STRUCTURE-MECHANICS RELATIONS OF LITHIUM BOROPHOSPHATE GLASSES

### 4.1.1. STRUCTURE INFORMATION

We initially concentrate on lithium borophosphate (LiBP) glasses due to their relative chemical stability in air, which allows for well-controlled experimental characterization. To introduce variations in disordered structures, component-dependent structural changes are considered. Consequently, we prepared various glassy electrolytes with compositions $x$Li$_2$O-(100-$x$)(0.5B$_2$O$_3$-0.5P$_2$O$_5$) for $x$ values of 38, 40, 42.5, and 45, referred to as 38LiBP, 40LiBP, 42.5LiBP, and 45LiBP, respectively, using both experiments and MD simulations in our previous paper[64]. As depicted in Figure 4-1, the Raman spectra normalized by area for these compositions reveal distinct modifications. Specifically, the spectra indicate an increase in the presence of $(P_2O_7)^{4-}$ and $(B\text{-}O\text{-}P)^-$ groups (identified as band 6) alongside a reduction in the types of phosphate groups integrated with $BO_4$ units (noted in band 3) and polyphosphate chains designated as $(PO_3)_n^{-n}$ (shown in band 4), correlating with the rise in lithium content. By maintaining a constant ratio of $B_2O_3$ to $P_2O_5$ ($n(B_2O_3)/n(P_2O_5) = 1$), adding lithium to the mix alters the glass network, leading to a less compact structure. This change facilitates the depolymerization of more polyphosphate chains, thereby enhancing the proportion of $(P_2O_7)^{4-}$ groups.

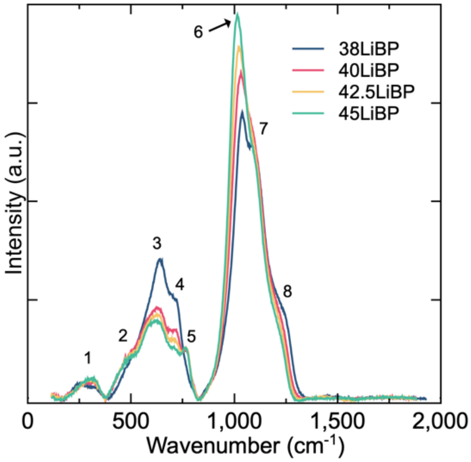

Figure 4-1 Raman spectra of the LiBP glassy electrolytes obtained by melt-quenching experiments. Area normalization and background correction were applied to the produced spectra. Figure reproduced from Paper I.

To investigate the atomic structure of LiBP glassy electrolytes, we used X-ray total scattering to analyze their short-range and medium-range structures. Figure 4-2 and our previous study[64] compares the experimental and simulated structure factor $S(q)$ and differential correlation function $D(r)$. The diffuse scattering observed in $S(q)$ from both experimental data and MD simulations demonstrates the absence of long-range order in LiBP glassy electrolytes. The experimentally obtained differential correlation function closely aligns with MD simulation results (38LiBP), yielding an $R\chi$ (introduced by Wright[65] to evaluate the degree of agreement between experimental and simulated PDFs) value of 5.1%. While the bond lengths of Li-O, P-O, and O-O remain relatively unchanged with varying lithium content, an increase in lithium content results in a shorter B-O bond length. This suggests a partial shift in boron coordination from $BO_4$ to $BO_3$ units, as evidenced by the reduced boron coordination number from MD simulations and the alteration of the O-B-O bond angle to around 120°. A similar transition from $BO_4$ to $BO_3$ with composition was previously observed in NMR studies of sodium borophosphate glasses[66].

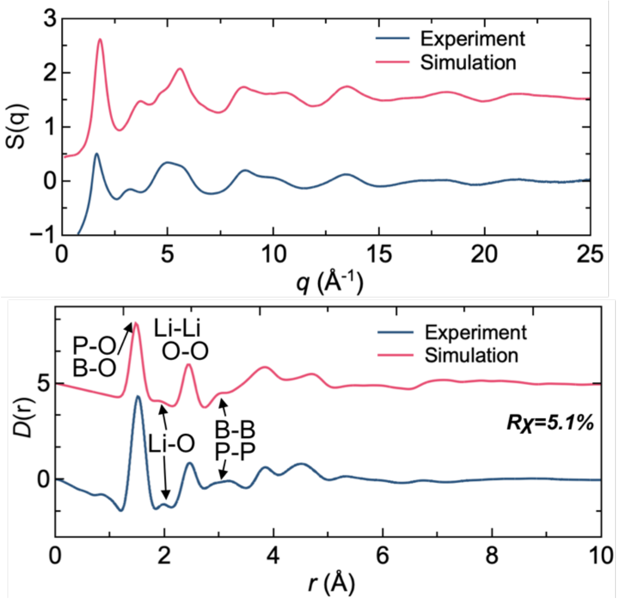

Figure 4-2 Comparison of the experimental (blue) and simulated (red) $S(q)$ and $D(r)$ for the 38LiBP glassy electrolyte. Figure reproduced from Paper I.

### 4.1.2. MECHANICAL PROPERTIES

The solid electrolyte may deform due to internal forces. The composition-dependent elastic characteristics of LiBP glassy electrolytes are shown in Table 4-1. Young's modulus ($E$) falls with increasing lithium concentration, indicating that the LiBP glass gets softer. This observation is supported by both experimental data and MD simulations. The reduction in Young's modulus corresponds with the observed decrease in Vickers hardness ($H_v$).

Table 4-1 Density ($\rho$), Young's modulus ($E$), Poisson's ratio ($\nu$), hardness ($H_v$), and fracture toughness ($K_{Ic}$) of LiBP glassy electrolytes obtained by experiments (Exp.) and MD simulations (Sim.).

| **Glass** | **$T_g$ (°C)** | **$\rho$ (g/cm$^3$)** | | **$E$ (GPa)** | | **$\nu$ (-)** | | **$H_v$ (GPa)** | ***CR* (N)** | **$K_{Ic}$ (Mpa·m$^{0.5}$)** | |
|---|---|---|---|---|---|---|---|---|---|---|---|
| | Exp. | Exp. | Sim. | Exp. | Sim. | Exp. | Sim. | Exp. | Exp. | Exp. | Sim. |
| **38LiBP** | 448 | 2.460 | 2.310 | 73.8 | 94.0 | 0.237 | 0.236 | 7.42 | 0.68 | 0.759 | 0.596 |

| | | | | | | | | | | | |
|---|---|---|---|---|---|---|---|---|---|---|---|
| **40LiBP** | 447 | 2.460 | 2.307 | 72.8 | 92.3 | 0.228 | 0.225 | 6.90 | 1.17 | 0.728 | 0.586 |
| **42.5LiBP** | 438 | 2.455 | 2.293 | 71.9 | 87.8 | 0.224 | 0.238 | 6.87 | 1.40 | 0.616 | 0.569 |
| **45LiBP** | 437 | 2.451 | 2.278 | 68.9 | 84.8 | 0.256 | 0.245 | 6.81 | 1.36 | 0.560 | 0.520 |

An important factor in extending the lifespan of solid-state electrolytes is minimizing crack formation, as cracks hinder ion transport. Crack resistance (CR) serves as a valuable measure for this. Figure 4-3 shows the load-dependent probability of crack initiation for four different LiBP glassy electrolytes. CR is assessed by counting the number of corners where indentation cracks occur. Variations in CR across different compositions are difficult to detect, especially under low loads. LiBP glasses, on the other hand, usually fracture at relatively low loads, with CR of around 1 N, which is lower than that of the majority of other oxide glass types[67],[68], as Figure 4-3 illustrates. This implies that under high local loads, LiBP glasses are very prone to cracking.

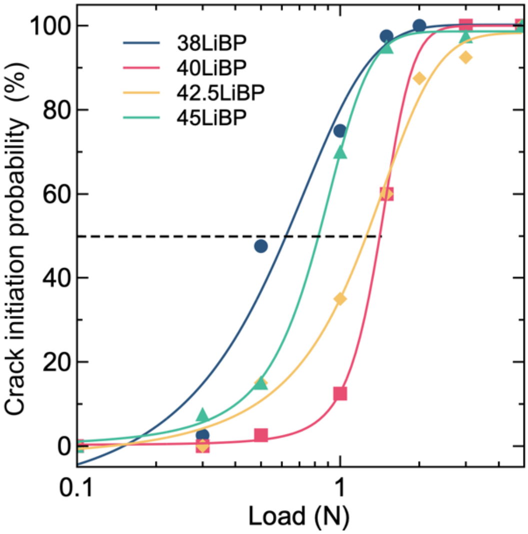

Figure 4-3 Probability of crack initiation in glassy LiBP electrolytes. Crack resistance (CR) can be defined as the stress at which 50% of crack initiation occurs. Figure reproduced from Paper I.

When solid-state electrolytes develop cracks, the battery's ability to function is significantly reduced and may potentially fail as a result of the cracks spreading further. Fracture toughness, $K_{Ic}$, quantifies the resistance of solid materials to crack propagation and is increasingly critical for evaluating solid-state battery performance. We measured the f $K_{Ic}$ of LiBP glassy electrolyte using the modified SEPB method. The sample was first given a pre-crack using a bridge compression fixture, and then a full fracture was induced. The pre-cracked LiBP glass electrolyte specimen's load-displacement curve during the fracture process is shown in Figure 4-4. The three-point bending fixture for the fracture specimen is depicted in Figure 4-4's upper right corner. Because it restricts stress corrosion[57], unstable fracture happened at $P_{max}$, which is crucial for determining $K_{Ic}$ based on the peak load.

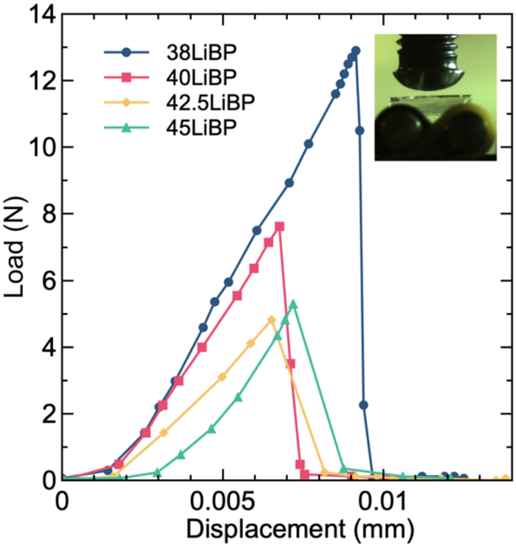

Figure 4-4 The three-point bending test load-displacement curve for LiBP glasses. A picture of the fractured specimen, obtained from one of the five standard 38LiBP specimens, is displayed in the upper right corner. Figure reproduced from Paper I.

### 4.1.3. MD SIMULATIONS

Figure 4-5a illustrates the simulated fracture process, where continuous bond stretching is observed near the crack tip. This method produces stress-strain curves (Figure 4-5b) that are used to determine $K_{Ic}$. LiBP glassy electrolytes exhibit a brittle mechanical response under load, with almost no ductile behavior, even at the nanoscale.

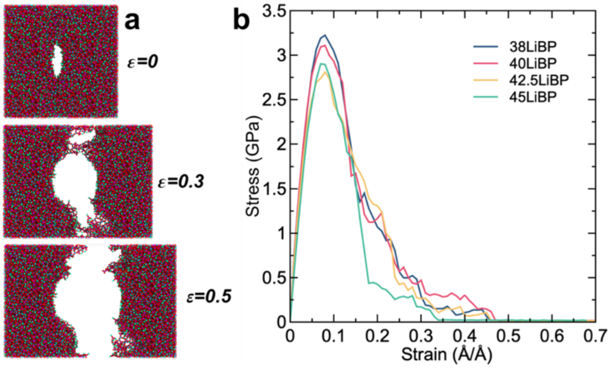

Figure 4-5 (a) Atomic snapshots of the LiBP glassy electrolyte's simulated fracture process at various strain levels. Green, blue, purple, and red spheres stand in for Li, B, P, and O, in that order. (b) The stress-strain curves as determined by MD simulations. Figure reproduced from Paper I.

A qualitative agreement of $K_{\mathrm{Ic}}$ calculated from both SEPB experiments and MD simulations is obtained as presented in Figure 4-6. Both experimental and simulation results indicate that $K_{\mathrm{Ic}}$ decreases with the increase in lithium content. Specifically, SEPB test results show that $K_{\mathrm{Ic}}$ values decline from 0.76 to 0.56 MPa·m$^{0.5}$ as lithium content rises from 38 to 45 mol%. This low $K_{\mathrm{Ic}}$ implies that the resistance to crack propagation diminishes with higher lithium content. Notably, there is a significant reduction in fracture toughness despite the relatively minor change in composition. Consequently, we employ MD simulations for pinpointing the critical structural evolutions occurring under load to better explain this phenomenon.

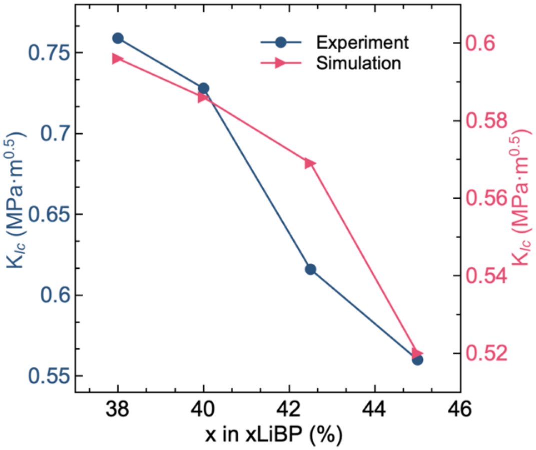

Figure 4-6 $K_{\mathrm{Ic}}$ values obtained from experiments and simulations. Figure reproduced from Paper I.

During fracture, energy dissipation is facilitated by the breaking and reformation of bonds, a process known as bond switching[69]. Figure 4-7 depicts the bond switching behavior of boron, highlighting events where the coordination number (CN) decreases, increases, or swaps under stress. When strained, the CN of the central boron atom can change in three ways compared to the unstrained state: (i) decrease from 4 to 3 (decreased CN), (ii) increase from 3 to 4 (increased CN), or (iii) retain the same CN but alter the surrounding oxygen atoms (swapped CN). This bond switching mainly involves transitions between $BO_3$ and $BO_4$ units and swapping of atoms within these units. As shown in Figure 4-7a, events of decreased CN surge at the onset of tensile stress, peak, and then level off after fracture. Increased and switched CN events are shown to be rising during the fracture process in Figures 4-7b and 4-7c. Glass relaxation is responsible for the increase in the frequency of increased CN events following fracture. These observations are consistent with previous studies[70,71]. Furthermore, the proportion of atoms experiencing bond switching decreases with higher lithium content in LiBP glassy electrolytes. The decline in atoms capable of bond switching (and thus stress release) is the main structural reason for reduced fracture toughness. Structural analysis shows that as lithium content increases, the CN of boron decreases, limiting the dissipation of fracture energy via CN reduction. This is evidenced by the larger fraction of atoms undergoing CN decrease compared to those involved in increased or swapped CN events[64].

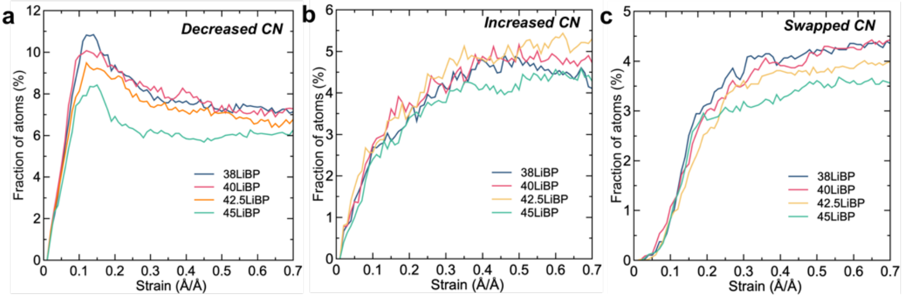

Figure 4-7 Bond switching events of boron atoms observed under load. Figure reproduced from Paper I.

### 4.1.4. STRUCTURAL DESCRIPTOR FROM MACHINE LEARNING

Machine learning presents a promising avenue for uncovering hidden patterns in multidimensional data, enabling the prediction of dynamics in disordered materials (such as fracture behavior) from structural features[71–73]. Various machine learning algorithms have been employed for this purpose, including support vector machines[73], logistic regression[74], graph neural networks[75], convolutional neural networks[76], and others. In particular, the structural fingerprint referred to as “softness”, proposed by Cubuk et al.[73,77], is closely related to the tendency of individual atoms to reorganize in accordance with their surroundings.

Beginning with the mechanical properties of disordered electrolytes, we utilized molecular dynamics (MD) simulations to study the LiBP glassy electrolyte, composed of $(Li_2O)_{40+x}(B_2O_3)_{30}(P_2O_5)_{30-x}$ (where $x$ equals -10, -5, 0, 5, and 10) as stated in our previous study[78]. First, we evaluated the LiBP electrolytes' mechanical response to a tensile load. Figure 4-8a illustrates the stress-strain curves for compositions with a fixed $B_2O_3$ content. As anticipated, increasing the $Li_2O$ content depolymerizes the glass network, resulting in decreased strength and ductility. Conversely, glasses with a fixed $Li_2O$ content show no significant composition dependence in their mechanical response[78]. Fracture processes generally involve changes in chemical bonds, so the concept of bond-switching is relevant for analyzing fracture behavior[69]. Crack initiation and propagation are included in the fracture of LiBP glasses, as Figure 4-8b illustrates. The sample is nearly entirely fractured at a strain of 0.4, with only a few B-O and P-O bonds bridging the crack. Three different forms of boron bond-switching events are shown in Figures 4-8c-e. For boron atoms, bond-switching can occur in the form of swapped, increased, and decreased CN relative to the non-strained structure. Figure 4-8c indicates that decreased CN events initially rise with applied strain but then diminish and stabilize as fracture begins. The increased and swapped CN events continuously rise with strain, attributed to glass relaxation[78]. This relaxation occurs as stress release from brittle fracture leads to partial re-densification of the glass, resulting in more increased and swapped CN events[78]. Overall, the likelihood of bond-switching decreases with higher $Li_2O$ content in the glassy LiBP electrolytes[78]. The next objective is to predict the mechanical behavior from the non-strained glass structure, using the probability of bond-switching in boron atoms.

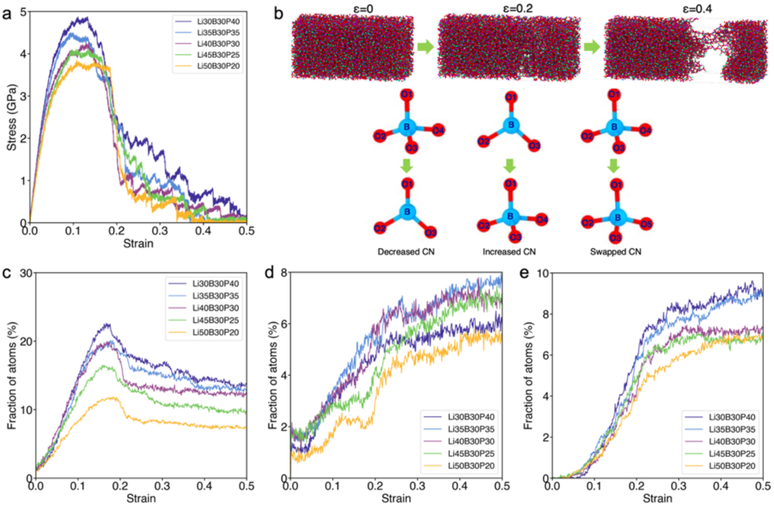

Figure 4-8 (a) Stress-strain curves with a constant $B_2O_3$ content for glassy LiBP electrolytes. (b) Atomic pictures of the three different kinds of bond-switching behaviors and the fracture process for the composition Li40B30P30 at different strain levels. (c-e) Fraction of boron atoms in glasses with fixed $B_2O_3$ concentration that experience (c) decreased CN, (d) increased CN, and (e) swapped CN depending on applied strain. Figure reproduced from Paper II.

The likelihood of boron atom bond switching ($P_{BS}$) is connected with the fracture behavior of LiBP glassy electrolytes. We looked into whether the static glass structure could predict boron's tendency to switch CNs. We used logistic regression to create a hyperplane that divides atom mobility according to structural characteristics using the softness approach described by Cubuk et al.[77] (Figure 4-9a). Softness ($S$) is calculated as the distance between this hyperplane and the location in feature space; a positive value indicates a mobile atom, and an absolute value indicates the possibility of mobility. Further details are available in Paper II[79]. Our findings show that boron atoms with higher $S$ values are more likely to undergo bond switching during glass deformation. Figure 4-9b displays the $S$ distribution of boron atoms in glasses with fixed $B_2O_3$ content, showing a bimodal characteristic. The peaks at $S$ values of -0.4 and 0.6 show that the boron atoms behave differently whether they are stationary and mobile. This bimodal distribution is caused by distinct coordination states of boron atoms, with $^{[4]}$B atoms being more prone to bond switching than $^{[3]}$B atoms, as shown in the inset of Figure 4-9b. $S$ for boron atoms is often reduced as the $P_2O_5$ level drops because the proportion of stationary boron atoms rises while that of mobile boron atoms falls. This explains why higher $P_2O_5$ content LiBP glasses tend to have more bond swapping, which improves their nanoscale ductility. Notably, even though the machine learning model's input structural features did not directly get the coordination information, the computed softness successfully represents the many dynamic behaviors arising from these coordination states.

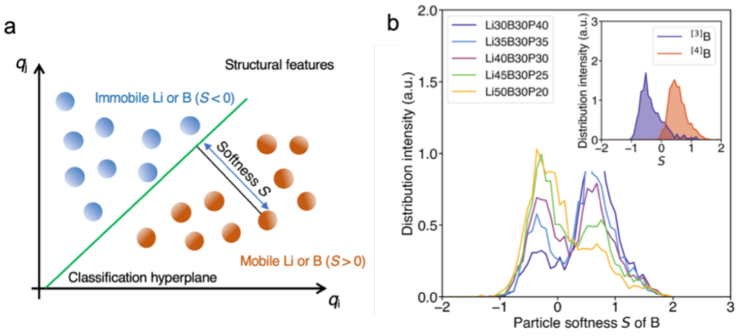

Figure 4-9 (a) Schematic of the classifier hyperplane used to determine atomic mobility: boron atoms with high mobility are prone to bond-switching after deformation, while lithium atoms with high mobility tend to diffuse spontaneously. (b) Intensity distribution of atomic softness for boron in electrolytes with fixed $B_2O_3$ content. The inset shows the distribution of softness values for $^{[3]}$B and $^{[4]}$B in the Li40B30P30 glassy electrolyte. Figure adapted from Paper II.

Lastly, we investigate how the fracture process modifies the atoms of boron's $S$. At intervals of $\Delta\varepsilon = 0.01$, the softness is computed as a function of applied strain. Despite the lack of specific sample information for constructing the classification hyperplane, the computed softness accurately captures the mechanical characteristics of the glassy LiBP electrolytes. Different softness values of boron atoms are consistently distributed in the undeformed sample, as shown in Figure 4-10a. The softness of boron often diminishes with deformation to $\varepsilon = 0.2$, especially in the vicinity of the crack zone. The average atom $S$ of boron in simulated LiBP samples as a function of strain is displayed in Figure 4-10b. Higher $P_2O_5$ content glasses typically have boron atom softness values that are higher, indicating a larger tendency for bond flipping. Softness can be used as a marker of the course of a fracture because it first reduces during stretching and then increases after reaching the fracture strain.

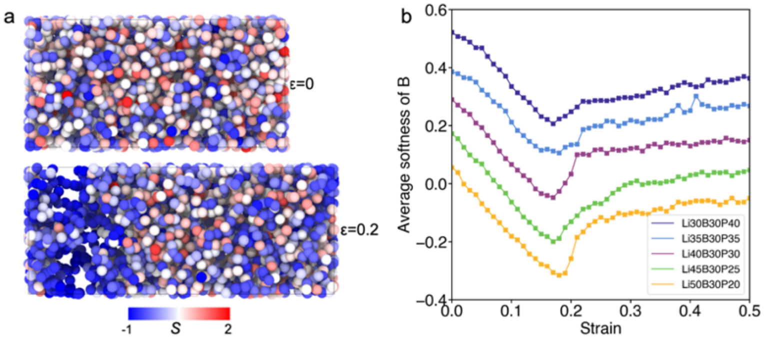

Figure 4-10 Relationship between strain and the softness of boron atoms. (a) The softness of boron atoms distributed spatially at various strain levels. The softness values of the boron atoms are used to determine their color coding. (b) The average atom softness of boron in different LiBP glassy electrolytes under load. Figure reproduced from Paper II.

## 4.2. STRUCTURE-MECHANICS RELATIONS OF LATP GLASS-CERAMICS

One of the most critical properties of solid electrolytes is ionic conductivity. Glass-ceramics, obtained through partial crystallization of glass, can enhance ionic conductivity by several orders of magnitude compared to their glassy or crystalline states. However, whether glass-ceramics can overcome the brittleness and low fracture toughness of their original glass structure, that is, their ability to resist crack propagation, remains insufficiently understood. LATP glass-ceramics are among the most promising solid electrolytes, with ionic conductivity ranging from $10^{-4}$ to $10^{-3}$ $S \cdot cm^{-1}$ at room temperature[79]. This section will continue to explore glass-ceramic electrolytes obtained from partial crystallization of glass, specifically LATP glass-ceramics, and the relationship between their structural changes and mechanical properties using classical MD simulations[79].

We begin by evaluating the effect of crystal content in glass-ceramics on their mechanical properties. Glass-ceramics are designated based on their crystal volume percentage, such as LATP-GC15 for a glass-ceramic containing 15% crystal content. In this nomenclature, LATP-G refers to the LATP glass, and LATP-C to the LATP crystal. Figure 4-11a displays stress-strain curves from uniaxial tensile tests for LATP glass-ceramics with various nanograin sizes. The crystal orientation in the LATP-C sample is consistent with the nanograins in the glass-ceramic. Our findings indicate that the mechanical properties of the LATP crystal are dependent on its orientation. As discussed in Paper IV[79], rotating the crystal by 90 degrees decreases both its modulus (slope of the stress-strain curve before 0.01 strain) and its fracture energy (area under the stress-strain curve). For further analysis, we selected the orientation with the higher modulus. Young's modulus, which is represented by the beginning slope of the stress-strain curves, rises with increasing crystal concentration (bigger nanograins) in glass-ceramics. According to Figure 4-11b, the computed modulus of the LATP crystal in this orientation is 139.1 GPa, which is in line with first-principle and experimental calculations (107-150 GPa)[80,81]. LATP samples generally show brittle fracture, which is defined by abrupt and total failure as soon as a crack starts. However, as Figure 4-11b illustrates, glass-ceramics with bigger nanograins exhibit higher fracture energy and better resistance to crack propagation. LATP glass-ceramics do not attain the crystalline phase's modulus, despite having a greater Young's modulus than the precursor glass. This is explained by the glass-ceramics' comparatively low crystallinity, with crystal content of no more than 25%. In spite of this, the glass-ceramics show superior fracture energy compared to the crystalline and pure glass phases.

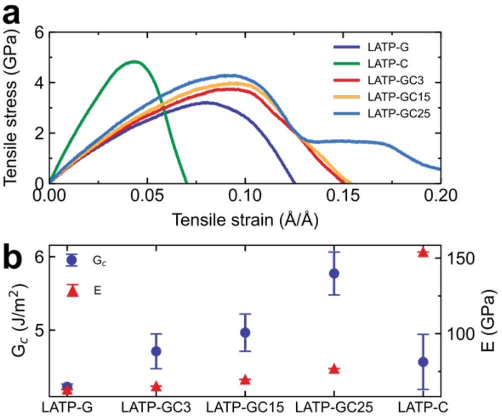

Figure 4-11 Stress-strain curves from the uniaxial tensile tests (a) and the corresponding fracture energy $G_c$ and Young's modulus $E$ values (b) for various samples. The crystal orientation in the LATP glass-ceramics is aligned with that in the LATP-C sample. Figure reproduced from Paper IV.

MD simulations shed light on atomic-scale structural alterations. We also investigated the LATP glass-ceramics' atomic-scale microstructure during fracture. As shown in Figure 4-12a, the effect of shear deformation is not limited to the area around the fracture; rather, it is mostly concentrated at the interface at which the contact area of crystal and glass phase (also known as the complexion layer). Through monitoring structural alterations under load, it is evident that microcracks occur and interfacial connections break. Furthermore, as shown in Figure 4-12b, the propagating cracks do not avoid any crystals; rather, they cause cleavage fracture by extending the crack route along the cleavage surface due to the nanograins.

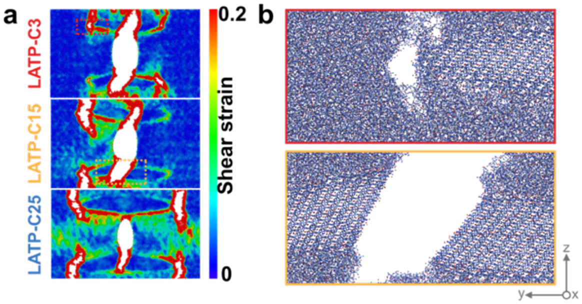

Figure 4-12 (a) Shear strain distribution in LATP glass-ceramics with a 0.15 strain. The current shear strain values of each atom with respect to the non-strained sample are represented by a color code. (b) Atomic snapshots of the LATP-GC3 (top) and LATP-GC15 (bottom) electrolytes under a strain of 0.15, displaying microcracks and cleavage fractures. Figure reproduced from Paper IV.

Next, we examine the process of bond breaking and reformation during tensile deformation. The variations in Al and Ti's total CN during the tensile process are shown in Figure 4-13. Since the phosphorus CN does not vary, the P-O pairs are not taken into account. As strain increases, Al-O and Ti-O's CNs decrease in disordered and partially ordered samples, reaching their minimum at the fracture beginning (around 0.1 strain), which indicates significant bond breakage occurring between 0 and 0.1 strain (Figures 4-13a-b). At a strain of roughly 0.15, the LATP-G sample totally fractures, and the relaxation of the post-fracture structure is what causes the CN changes that follow. The CNs increase when new fracture surfaces are formed and bonds repair during the rapid crack propagation and eventual fracture. This process continues until full fracture occurs at strains greater than or equal to 0.15. Therefore, the CNs of Al-O and Ti-O vary in glass and glass-ceramic systems. But in LATP crystals, the CN of Ti stays rather constant with increasing strain, while the CN of Al only reaches a minimum at the beginning of fracture (Figure 4-13c).

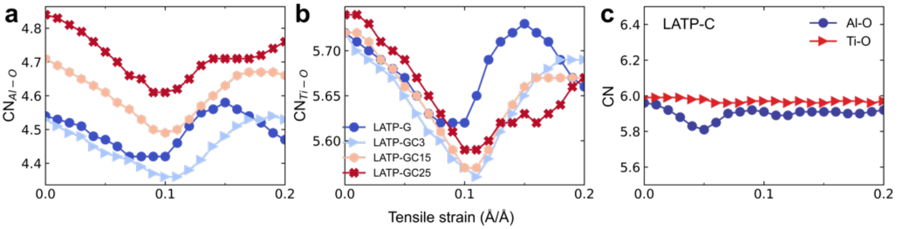

Figure 4-13 Changes in coordination numbers (CN) for Al–O and Ti–O in LATP electrolytes during loading process. Panels (a) and (b) display these changes in glass and glass-ceramic sample, respectively, panel (c) presents the results for the crystal. Figure reproduced from Paper IV.

The average changes in CN were not sufficient to infer the bond switching events. As a result, we additionally analyze each atom's coordination environment in relation to its non-strained state[69,70], categorizing them into four types as described before. Figure 4-14 presents the proportion of these bond switching events for Al-O.

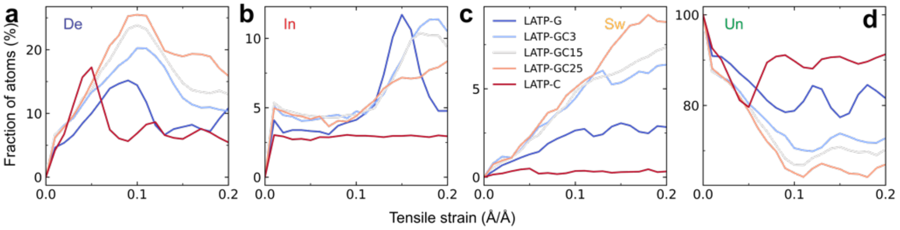

Figure 4-14 The proportion of Al-O bond switching events under load is categorized into decreased CN, increased CN, exchanged CN, and unchanged CN. Figure reproduced from Paper IV.

Overall, larger nanograins in LATP lead to increased bond switching events, with LATP-GC25 showing the highest activity. During the loading process, Sw-events rise steadily in glass and glass-ceramics. In LATP crystals, where In events are almost nonexistent and De-events are more common, this tendency is not observed. Ti-O's bond switching behavior resembles that of Al-O in comparable ways[79] (Paper IV). Increased crystal content in the glass-ceramics results in more bond switching events, evidenced by the decreasing fraction of Un events. Although the crystalline phase in LATP-C exhibits relatively few bond switching activities (Figure 4-14d), the partially crystalline glass-ceramics display higher bond switching events and increased fracture energy (Figure 4-11b) as the crystalline phase content rises.

# CHAPTER 5. STRUCTURE AND ION DYNAMICS RELATIONS

In this chapter, we study the mechanisms of ion diffusion in disordered electrolytes. Ion hopping events in solids occur at the atomic scale, and molecular dynamics simulations using classical potential functions, as well as more accurate machine learning potential functions, are employed to simulate disordered electrolytes. We conducted classical molecular dynamics simulations (rather than AIMD) to obtain glass structures containing thousands of atoms for sampling numerous hopping events. Lithium thiophosphate (LiPS) glassy electrolytes, known for their high ionic conductivity, are chosen as the subject of study, along with glass-ceramics obtained through partial crystallization of the same compositions. The rich structural information of these disordered or partially disordered electrolytes will be linked to the dynamics of lithium-ion migration.

## 5.1. LI$_2$S-P$_2$S$_5$ GLASSY ELECTROLYTES

### 5.1.1. STRUCTURAL CONSTRUCTION

Sulfide-based inorganic solid electrolytes, specifically lithium thiophosphates ($Li_2S$-$P_2S_5$), belong to the thiophosphate LISICON (lithium superionic conductor) and are known for their high ionic conductivity[82,83]. For instance, $70Li_2S$–$30P_2S_5$ glass-ceramics exhibit an ionic conductivity of $1.7 \cdot 10^{-2}$ S·cm$^{-1}$ at room temperature[84]. In $Li_2S$-$P_2S_5$, three primary anion clusters are present: $P_2S_6^{4-}$, $P_2S_7^{4-}$ and $PS_4^{3-}$. Figure 5-1 depicts the P-P bond in the $P_2S_6^{4-}$ cluster, the corner-sharing $P_2S_7^{4-}$ tetrahedral pairs, and the $PS_4^{3-}$ tetrahedral cluster. By using Raman spectroscopy and $^{31}P$ nuclear magnetic resonance spectroscopy[34,36,85], LiPS electrolytes has been characterized. According to these research, glasses of the same composition may include varying amounts of local structures, and different glass compositions show notable differences in their local polyatomic structures[86]. Not only do significant structural differences arise in disordered and partically disordered forms produced by different processes (such as heat treatment, mechanical ball milling, or melt quenching), but they also exist in samples created by the same process.

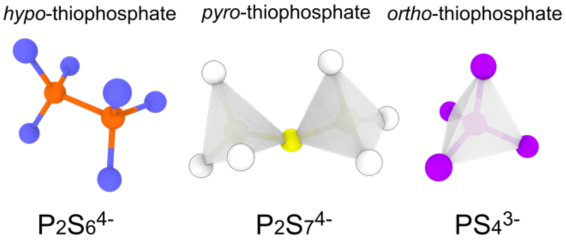

Figure 5-1 Schematic representation of polyatomic anions in LiPS glass electrolytes. Figure reproduced from Paper III.

We have gathered structural data on LiPS glasses from both the literature and our measurements (Figure 5-2). The interatomic potential from ref.[87] was chosen not only for the reproduction of structural features and ionic conductivity (in comparison with experimental and AIMD results[87]), but also we adjust the local structure content to align with those reported in the literature for LiPS glassy electrolytes as stated in our previous paper[88].

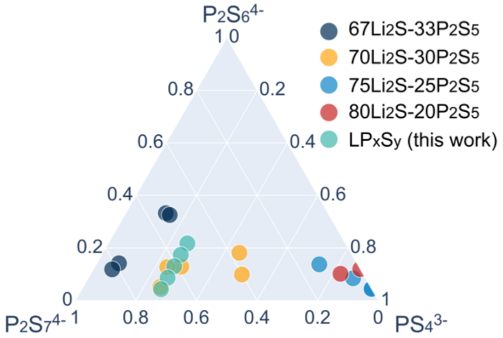

Figure 5-2 Ternary diagram presenting the content of $P_2S_6^{4-}$, $P_2S_7^{4-}$, and $PS_4^{3-}$ units in the $Li_2S$-$P_2S_5$ glassy electrolytes system. Figure reproduced from Paper III.

Specifically, we simulated five different compositions of $P_2S_6^{4-}$ and $P_2S_7^{4-}$ contents within the $Li_2S$-$P_2S_5$ glassy electrolyte system, maintaining an approximate $Li_2S$-to-$P_2S_5$ ratio of 7:3. We simulated the glassy electrolyte with the chemical formula $LiP_xS_y$, where $x$ is equal to 0.465 and y ranges from 1.605 to 1.651. The lithium content was constant in all system[88]. Based on the local environment of the different atoms, we calculated the RDF $g(r)$. The left panel of Figure 5-3 shows $g_{P\text{-}S}(r)$, indicating that the bond lengths of P-S are approximately 2.1 Å for all three clusters. In $P_2S_6^{4-}$, the distance between P and S is in the range of 3.4-3.8 Å due to the presence of P-P bonds. Right figure on the Figure 5-3 presents the RDF of Li-S in $P_2S_6^{4-}$, $P_2S_7^{4-}$ and $PS_4^{3-}$, showing no significant change in the distance of Li-S, that is, lithium is located evenly around the three clusters.

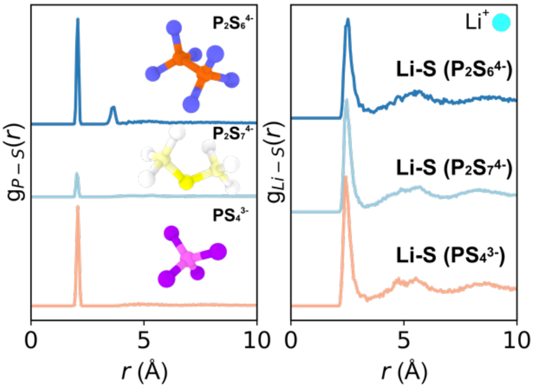

Figure 5-3 Partial radial distribution functions *g*(*r*) for P-S (left) and Li-S (right) in the anionic cluster. Figure reproduced from Paper III.

### 5.1.2. IONIC CONDUCTIVITY

As we varied the relative contents of $P_2S_6^{4-}$, $P_2S_7^{4-}$ and $PS_4^{3-}$ in the LiPS glass, the tendency of diffusion coefficient of Li also changed. Figure 5-4 illustrates the relationship between temperature and the diffusion coefficient, which shows Arrhenius relation, and a reduction in the content of $P_2S_6^{4-}$ will lead to the decrease of activation energy $\Delta E$. Additionally, we observe a decrease in lithium diffusion capacity when there is an absence of S, which corresponds to an increased $\Delta E$. This suggests that a higher content of $P_2S_6^{4-}$, leading to a reduction in P-S bonds, may impede lithium conduction.

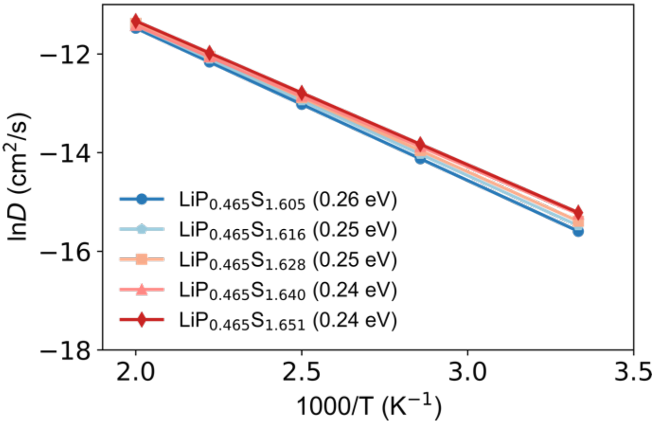

Figure 5-4 The lithium diffusion coefficient as a function of temperature. The activation energy, calculated from the slope of the Arrhenius fit, is indicated in parentheses. Figure reproduced from Paper III.

Using the diffusion coefficient, the ionic conductivity ($\sigma$) was calculated by Eq. (3.8). The orange-shaded area in Figure 5-5 displays the $\sigma$ of the LiPS glass in comparison with data from Refs[34,83,85,36]. Notably, the ionic conductivity in the $70Li_2S$-$30P_2S_5$ glass system varies significantly due to the different amounts of $P_2S_6^{4-}$, $P_2S_7^{4-}$ and $PS_4^{3-}$. The rotational dynamics of $PS_4^{3-}$ have previously been shown to facilitate lithium ion migration, known as the paddlewheel effect[89]. The $P_2S_6^{4-}$ anion clusters are considered unstable[90], the theoretical ionic conductivity for the $Li_4P_2S_6$ crystal is very low[37]. In the present glasses, a robust migration pathway for lithium near $P_2S_6^{4-}$ may be impeded by complex displacements of $P_2S_6^{4-}$ units. The observed increase in $\Delta E$ and decrease in $\sigma$ with a higher fraction of $P_2S_6^{4-}$ also suggest a possible hindrance mechanism caused by these units. Previous studies[36,91,92] proposed that the corner-sharing $P_2S_7^{4-}$ units tnhibit lithium conduction by shielding the positive charge of phosphorus caused by electron transfer between phosphorus and bridging sulfur. Another study found that the flexibility of $P_2S_7^{4-}$ di-tetrahedra promotes lithium-ion diffusion[93]. The complexed configuration of polyatomic anion clusters makes the mechanism of ion transport in the glass difficult to understand, requiring the use of advanced computational techniques[88].

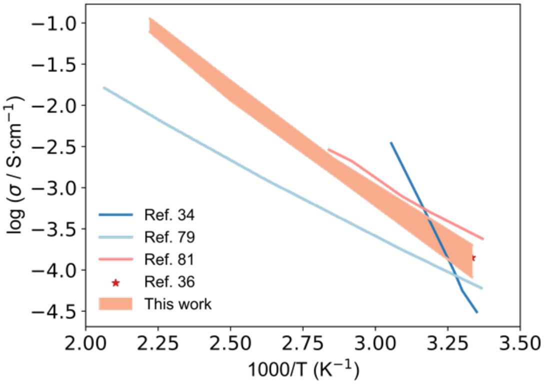

Figure 5-5 Ionic conductivity for LiPS glasses in this work (depicted by the orange-colored area). These results are compared to experimental and simulated ionic conductivity data for $70Li_2S$-$30P_2S_5$ glassy electrolytes, which feature varying content of polyatomic anions[34,83,85,36]. Figure reproduced from Paper III.

### 5.1.3. CORRELATING ION MOBILITY WITH STRUCTURE USING MACHINE LEARNING

We aim to understand how the spatial environment surrounding the $P_2S_6^{4-}$, $P_2S_7^{4-}$ and $PS_4^{3-}$ anions influence ion mobility in this system. To achieve this, we correlate local structure and dynamics using the concept of "softness"[71,72,74], and we used before to correlate bond switching and fracture behavior. By capturing atomic rearrangements through structural features, and possessing the softness to accommodate not only the coordination switching of atoms but also the rearrangements of lithium atoms. In detail, logistic regression[94] was used to construct a hyperplane based on the static structure at 300 K. Furthermore, we calculate each lithium ion's nonaffine square displacement $D^2_{min}$, a quantity that is frequently utilized to characterize atomic rearrangement events. Each lithium ion's degree of rearrangement is expressed as the cumulative sum of $D^2_{min}$ values across short time intervals ($D_{\mathrm{cum}}$).

All lithium ions are split into two types by the hyperplane: mobile (soft) and immobile (hard), which correspond to positive and negative $S$ values, respectively. The absolute $S$ of each particle is reflected in the distance from the hyperplane. In contrast to crystalline materials that possess unique ion transport channels[95], disordered structure results in a wide range of lithium mobility. The distribution of softness ($S$) in glasses with varying anion cluster contents is depicted in Figure 5-6, where a peak shift toward greater $S$ value is observed as the structure's $P_2S_6^{4-}$ and $P_2S_7^{4-}$ contents rise and fall, respectively.

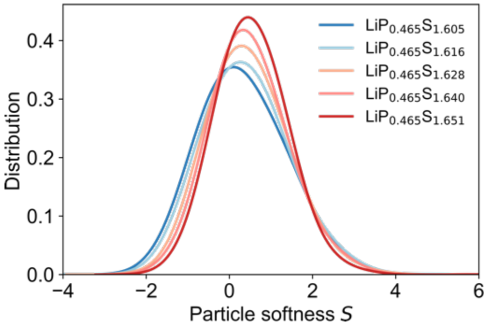

Figure 5-6 Distribution of particle softness for lithium in various LiPS glassy electrolytes. Figure reproduced from Paper III.

We suggest a relationship between the *S* values of lithium and the nearby polyatomic anions, since the immediate environment affects the conductivity of lithium. From Figure 5-7, it is evident that lithium ions near $PS_4^{3-}$ generally exhibit positive softness values, whereas those near $P_2S_6^{4-}$ predominantly show negative *S* values, indicating a strong spatial correlation. According to the Pearson correlation coefficients, there is a -96% association between the *S* value of lithium and the likelihood of discovering S atoms in $P_2S_6^{4-}$ clusters, and a +96% correlation with those in $PS_4^{3-}$ clusters.

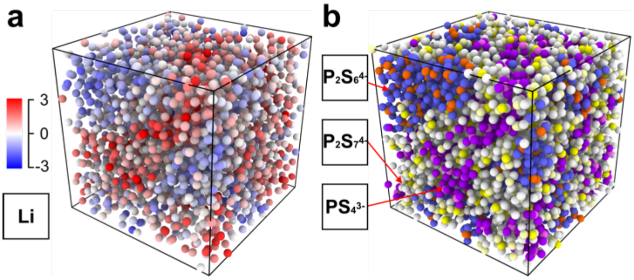

Figure 5-7 (a) Snapshot of lithium atoms in the $LiP_{0.465}S_{1.605}$ glass, which are color-coded by their *S* value. (b) Polyatomic anions in glassy $LiP_{0.465}S_{1.605}$, lithium atoms are hidden for a better comparison. Figure reproduced from Paper III.

To confirm this observation, we computed the RDF for Li-S, where S atom is part of various anions, as presented in Figure 5-8a. The RDF of Li-S shows the probability of finding a neighboring S atom in $P_2S_6^{4-}$, $P_2S_7^{4-}$ or $PS_4^{3-}$ at a distance *r* from a given Li atom. Figure 5-8b identifies the specific *S* distribution of lithium around different anions. This indicates that softness can serve as a measure of lithium mobility and affirms the significant correlation between lithium mobility and its local surroundings. It is important to note that *S* is determined only by the surrounding Li atoms, excluding neighboring P and S atoms. Consequently, the anions influence the spatial distribution of Li, thereby controlling the mobility of Li atoms.

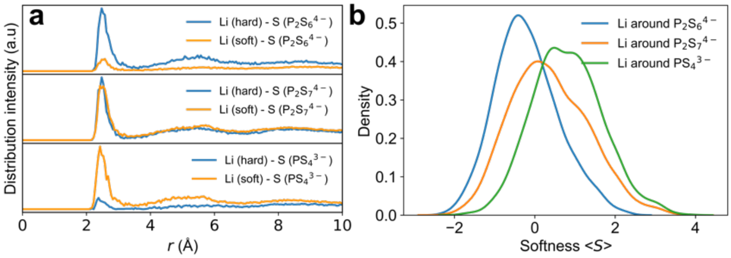

Figure 5-8 (a) Partial RDFs of Li-S pairs in the $LiP_{0.465}S_{1.605}$ glass. Li-S pairs show soft and hard lithium ions as blue and orange, respectively. (b) Softness distribution of lithium around different polyatomic anions within 5 Å (using $LiP_{0.465}S_{1.605}$ as an example). Figure reproduced from Paper IV.

Additionally, we observe that the potential energy (PE) and Voronoi volume of lithium are closely associated with their *S* value, as shown in Figure 5-9. Lithium-ions with larger softness tend to exhibit higher PE and larger Voronoi volumes. This correlation aligns with expectations, as both increased local free volume and instability (high energy) are likely to enhance the mobility of Li atoms.

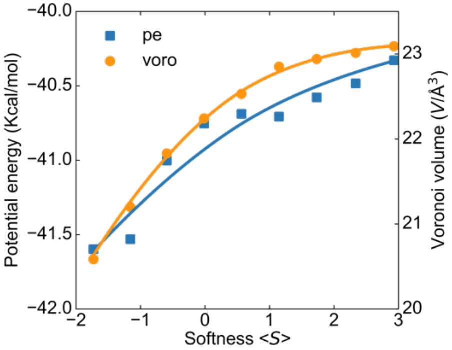

Figure 5-9 The averaged potential energy (pe, Kcal/mol) and Voronoi volume (voro, Å$^3$) of lithium plotted against their particle softness. Figure reproduced from Paper III.

### 5.1.4. CORRELATE SOFTNESS WITH ION DYNAMICS

We have shown that Li ions around $PS_4^{3-}$ exhibit high mobility, whereas the presence of $P_2S_6^{4-}$ units significantly hinder Li mobility. Next, the relationship between softness and ion dynamics were further investigated. Ion diffusion in solids is the hopping of individual ions inside the anions-formed crystal structure between ground-state stable sites and/or intermediate metastable sites (e.g., $O^{2-}$, $S^{2-}$, or polyatomic anion clusters)[15,95]. In disordered materials, the lack of regular coordination sites and symmetric long-range migration pathways complicates the establishment of conduction theory, but the hopping theory for mobile elements remains applicable. In order to solve this, the distribution of energy barrier for hopping ions in glasses must be determined statistically rather than discretely like in crystalline materials[15].

Ions travel across the energy landscape, as shown in Figure 5-10, with the diffusion energy barrier shown by the peak along the migration route. The nudged elastic band (NEB) method maps the energy landscape of each lithium ion and is widely used to find the energy barrier that the lithium ions must cross in order to migrate (5-10 Å away). Based on *S* of lithium, we divide lithium ions into two groups: soft lithium ($S > 0$) and hard lithium ($S < 0$).

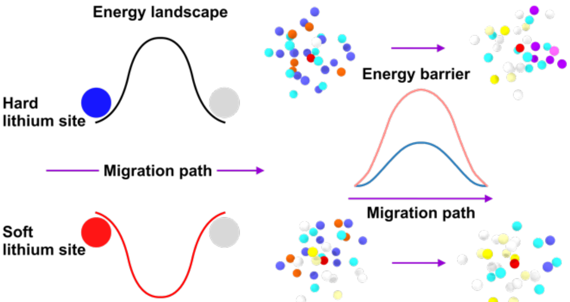

Figure 5-10 Schematic illustration of single Li-ion migration. Figure reproduced from Paper III.

We computed the energy barriers that lithium ions must cross in order to migrate between sites with different *S* values in order to learn more about this subject[88]. The energy profile of a single lithium-ion migration is shown in Figure 5-11a. Soft lithium ions encounter lower energy barriers when they migrate to a new location as shown in Figure 5-11b. This implies that whereas hard lithium ions are usually confined by their surroundings and require more energy to travel, soft lithium ions are more mobile and exist in a comparatively high energy state.

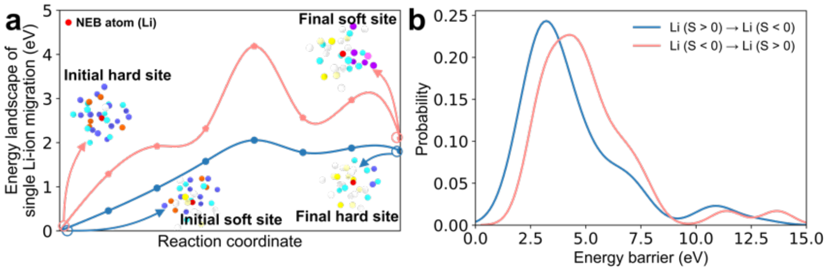

Figure 5-11 (a) Energy landscape of a single Li-ion migrating from an initial soft (hard) position to a final hard (soft) site, using $LiP_{0.465}S_{1.605}$ glass as an example. (b) Distribution of energy barriers for lithium migration. Figure reproduced from Paper III.

By monitoring the trajectories of lithium atoms around various anion clusters over a period of 10 ps at 500K, as shown in Figure 5-12, we observe that lithium ions tend to stay localized around $P_2S_6^{4-}$, resulting in reduced lithium mobility due to the relatively higher energy barrier. Conversely, lithium ions near $PS_4^{3-}$ show increased mobility and experience longer hopping events. Additionally, lithium ions surrounding $P_2S_7^{4-}$ demonstrate limited long-range movement. Considering that these lithium ions have near-zero $S$ values, it is inferred that their effect on lithium transport is likely minimal.

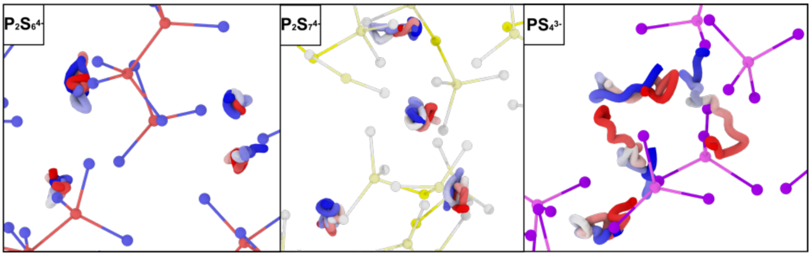

Figure 5-12 Trace of lithium's trajectory over a 10 ps simulation at 500 K in the $LiP_{0.465}S_{1.605}$ glass, with dark green indicating initial positions and bright green representing final positions. Figure reproduced from Paper III.

## 5.2. $LI_2S$-$P_2S_5$ GLASS-CERAMIC ELECTROLYTES

Uncertainty surrounds the precise mechanisms underlying ion diffusion in disordered or glassy solid electrolytes[15,19,20], largely due to the irregular energy landscape inherent to these materials[59]. The absence of a well-defined crystal lattice complicates the prediction and control of ion pathways. Moreover, the structural heterogeneity induced by defects and disorder further adds to the complexity of understanding ion conduction. Notably, the classical potential previously used, developed by Ariga et al.,[87] has shortcomings, especially when it comes to reactions and bond breakage. In the same way, Kim et al.'s classical potential [96] restricts bond breaking and is specific to $\gamma$-$Li_3PS_4$. To overcome these limitations, we developed a machine learning-based interatomic potential (MLIP)[97] using AIMD training data[98]. This MLIP was used to construct ordered, disordered, and partially disordered $Li_3PS_4$ electrolytes , allowing us to quantify structural descriptors for varying degrees of order and disorder[98].

### 5.2.1. STRUCTURAL DESCRIPTORS

We first examined the structural information for different degrees of disorder. Using molecular dynamics simulations, we modeled glass-ceramic sample $Li_3PS_4$. The glass-ceramic sample is snapshotted in Figure 5-13a, which provides a visual depiction of the distribution of disorder degree $F(\mathcal{Z})$ along the simulation cell's $y$-axis. As stated in our earlier work[98] and Ref.[46]. $F(\mathcal{Z})$ is computed using the Fourier transform method and the Gaussian density of atomic configurations. Briefly, we first map the coordinates of the simulated atoms onto a three-dimensional grid, then create density slabs of width $\Delta y$ along the $y$-axis of the simulation sample and project them into two dimensions The zero-frequency component is moved to the center and the two-dimensional discrete Fourier transform is applied to determine $F(\mathcal{Z})$. The specific formula is as follows:

$$F(z) = \frac{\sum_{xz} I_{\mathrm{2D-FFT}}(y)}{\sum_{xz} I_{max}}. \tag{5.1}$$

$F(\mathcal{Z})$ value is approaching 1 in a disordered structure and 0 in an ordered structure, the value between 0 and 1 indicates a transition in disorder level at the interface between the glass and crystal phases. This transition is shown in the $F(\mathcal{Z})$ profile as a double-minima curve. Figure 5-13b illustrates the corresponding profiles for element concentration and density. Using certain bin values from the simulated boxes, we compute the averages along the $y$-axis. These profiles show the periodic crystalline phase, whereas the glassy phase's homogeneity is highlighted. The interfacial phases are indicated by the gray rectangle, and a representative crystalline plane is indicated by the dashed line.

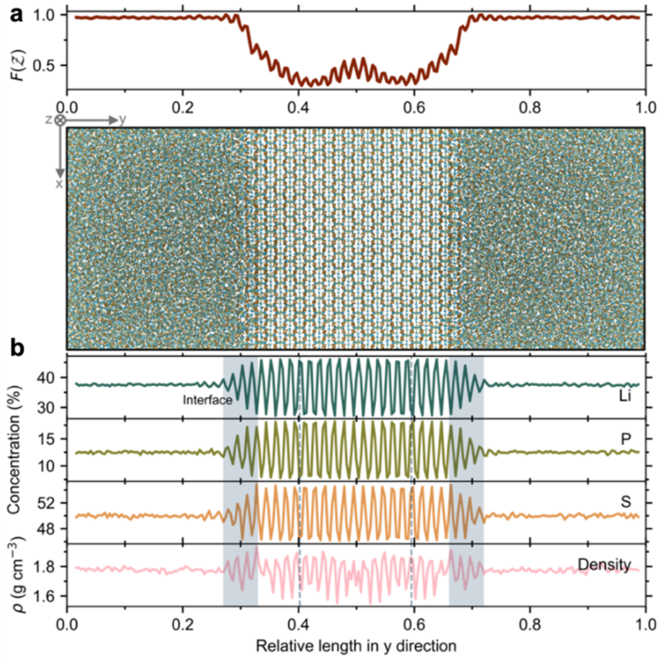

Figure 5-13 (a) $F(\mathcal{Z})$ distribution and corresponding atomic structure of glass-ceramic $Li_3PS_4$, $F(\mathcal{Z})$ shows the distribution of amorphization along the $y$-axis at the top. (b) Profiles of element concentration and density from atomic structure as shown in (a). Figure reproduced from Paper V.

Figure 5-14a shows the RDF of Li-S pairs, providing insights into ion interactions within $Li_3PS_4$ systems. Moreover, it contrasts the integrated RDFs for glassy $Li_3PS_4$, glass-ceramic $Li_3PS_4$, and crystalline β-$Li_3PS_4$. The distance distributions of Li and S do not change much even if the structures go from ordered to disordered, and Li still has a CN of about 4. Li is found in both tetrahedral and octahedral interstitial sites among the S atoms in the case of β-$Li_3PS_4$. Figure 5-14b displays the angular distribution function of S-P-S, illustrating the tetrahedral PS4 motifs formed between sulfur and phosphorus atoms, which sheds light on the local bonding states within the system.

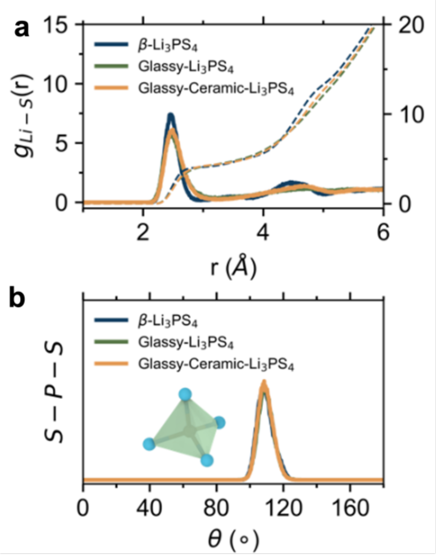

Figure 5-14 (a) RDFs of Li-S pairs and integrated RDFs for glassy-, β-, and glass-ceramic $Li_3PS_4$. (b) Angular distribution function of S-P-S. Figure reproduced from Paper V.

### 5.2.2. DYNAMICS OF HOPPING IONS

The effect of disorder on ions dynamics is assessed. We begin by evaluating the time-averaged mean-squared displacement (MSD, $\overline{\langle r^2(t)\rangle}$)of lithium ions (Figure 5-15). The MSD calculates the ions' average cumulative distance traveled. At elevated temperatures, the β-$Li_3PS_4$ electrolytes show the highest MSD values at 900 K (Figure 5-15) and 1000 K[98]. As opposed to the purely glassy $Li_3PS_4$, the glass-ceramic $Li_3PS_4$ exhibits a marginally lower MSD since it consists of both glassy and crystalline phases. At 1000 K, diffusion dynamics are observed in all $Li_3PS_4$ electrolytes, which ultimately reaching Fick's limit ($t^1$). The difference in the total migration of hopping lithium particles among β-$Li_3PS_4$ with both other forms steadily diminishes as the temperature reduces. To be more precise, at 700 K, the MSD for $Li^+$ in β-$Li_3PS_4$ becomes smaller than that of glassy and glass-ceramic $Li_3PS_4$ (see also in our paper[98]).

This reduction in MSD occurs as the temperature drops. It is interesting to note that a highly orderly structure, which includes a major movement channel joining octahedral and tetrahedral sites, exhibits a larger reduction in MSD with lowering temperature than the disordered structure, which is defined by isotropic transport pathways[99].

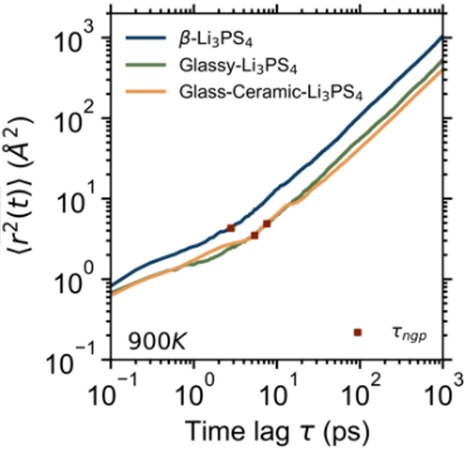

Figure 5-15 MSD of lithium ions for β-, glassy-, and glass-ceramic $Li_3PS_4$ systems varied with time lag, $\tau$. The NGP peak times are shown by red squares, $\tau_{ngp}$. Figure reproduced from Paper V.

While a particle's displacement distribution deviates from a Gaussian distribution, it is termed to demonstrate anomalous diffusion. Dynamic heterogeneity is commonly used to characterize the deviation of displacement to a Gaussian distribution[100]. We analyze anomalous diffusion across various $Li_3PS_4$ systems using the non-Gaussian parameter (NGP) $\alpha_2(t)$ descriptor to obtain a better understanding of the periodic behavior of lithium ions. The NGP, sometimes referred as the fourth cumulant of displacement, is a recognized indicator of dynamic heterogeneity and oscillations in the diffusion coefficient[101]. The degree that particle diffusion departs from Gaussian behavior is quantified. Lithium-ion mobility has non-Gaussian properties, as seen in Figure 5-16a, suggesting the phenomenon is not entirely random. Illustrating by $\tau_{ngp}$ (red squares), the NGP peak times indicate the presence of non-Gaussian dynamics. Peak heights of NGP peaks are higher and their appearance is delayed with increasing degrees of disorder. As illustrated in Figure 5-16b, where bigger atoms are employed to amplify displacements more than 4 Å, we highlight significant movements to emphasize the short time (10 ps) fluctuations in ions' displacement. Lithium ions are abundant within the disordered glassy phase, where they display larger displacements compared to those in the crystalline phase and rapidly diverge from their original vibrational locations.

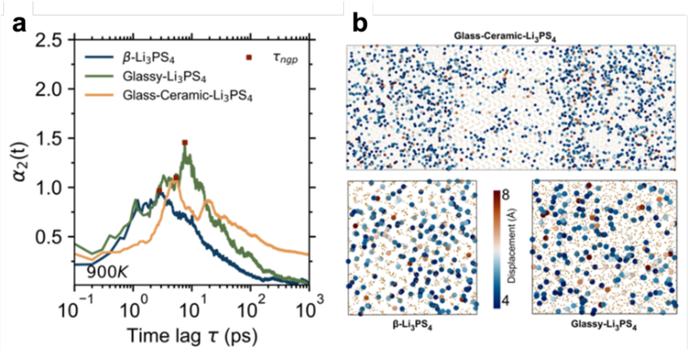

Figure 5-16 (a) Non-Gaussian parameter (NGP, $\alpha_2(t)$) of lithium ions for β-, glassy-, and glass-ceramic $Li_3PS_4$ systems. The NGP peak times, $\tau_{\mathrm{ngp}}$, are shown as red squares. (b) Short-term displacement of lithium for 10 ps. For improved depiction, bigger markers are used to indicate displacement magnitudes greater than 4 Å. Figure reproduced from Paper V.

Overall self-part van Hove correlation function ($G_s$) of Li-Li pairs for the different $Li_3PS_4$ systems is shown in Figure 5-17 to help explore the relationship between particle mobility from short- to long-time behaviors in more detail. The function $G_s(r,t)$ describes the Li-Li pair separation distance $r$ at time $t$, while $r^2G_s(r,t)$ represents the particle displacements' probability distribution[102]. Figure 5-17a shows that β-$Li_3PS_4$ exhibits higher probabilities for long-range displacements (>10 Å) as time progresses. The prolonged migration of hopped ions along specific transport pathways within the crystal structure is the cause of this behavior[99]. Glassy $Li_3PS_4$, on the other hand, performs worse due to the complicated migration pathways of its disordered structure. It's interesting to note that glass-ceramics $Li_3PS_4$ do not show a movement distribution between the crystal and glassy electrolytes. This phenomenon can be explained by the orientation of crystalline phases, as hopping ions in β-$Li_3PS_4$ tend to follow a preferred diffusion direction along the *c*-axis on the *ac*-plane[99] (i.e., the *z*-direction in Figure 5-13a). When observing the probability distribution over a set time interval between 1 and 10 ps (Figure 5-17b), the glass-ceramic $Li_3PS_4$ shows a broad, single peak centered around 1 Å, influenced mainly by equilibrium vibrations and nearest-neighbor site occupation[102]. Remarkably, β-$Li_3PS_4$ shifts from a single peak to a split peak in less than 10 ps, suggesting that these ions are starting to migrate and move out of their initial equilibrium locations. In glassy $Li_3PS_4$, a minor shift in the $r^2G_s(r,t)$ distribution is also observed.

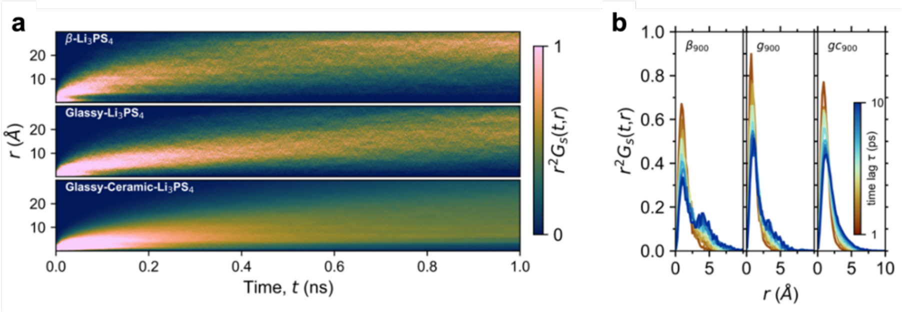

Figure 5-17 Self-part van Hove correlation function for β-, glassy-, and glass-ceramic $Li_3PS_4$ systems at 900 K for long time scale (1 ns) (a) and short time scale (b) between 1 and 10 ps. Figure reproduced from Paper V.

### 5.2.3. IONIC CONDUCTIVITY

Macroscopic ionic conduction results from the collective migration dynamics of ions within a material[19]. These dynamics are inherently linked to the material's structural characteristics. Here, we explore how the transition from ordered to disordered structures affects lithium-ion mobility and the resulting ionic conductivity. We start by examining the diffusion coefficient (*D*), derived from the slope of the MSD-time curve. The diffusion coefficient's temperature dependence, which exhibits an Arrhenius-type characteristic, is shown in Figure 5-18a. The degree of disorder affects this temperature dependency; this is seen in glasses and glass-ceramics as opposed to β-$Li_3PS_4$ by the reduced activation energy (derived from the slope). It is interesting to note that activation energies and ionic conductivities of glass-ceramic $Li_3PS_4$ electrolytes, which have somewhat ordered structures, are either slightly higher than or comparable to those of purely glassy $Li_3PS_4$ (Figure 5-18b). This enhancement in ionic conductivity due to ordering is consistent with previous findings for the $Li_3PS_4$ system[103–105] as well as for the $Li_2S$-$P_2S_5$ and $Li_7P_3S_{11}$ systems[83–85,106,107]. The Nernst-Einstein equation is used to compute the temperature-sensitive conductivity of ion for $Li_3PS_4$, and Figure 5-18b shows the results with respect to various ordered and disordered electrolytes. The simulated ionic conductivities with different levels of disorder closely resemble experimental values that have been reported in the past[82,108,109]. Above all, the ionic conductivity of the disordered $Li_3PS_4$ electrolytes is noticeably higher at room temperature than that of the β-$Li_3PS_4$ electrolytes.

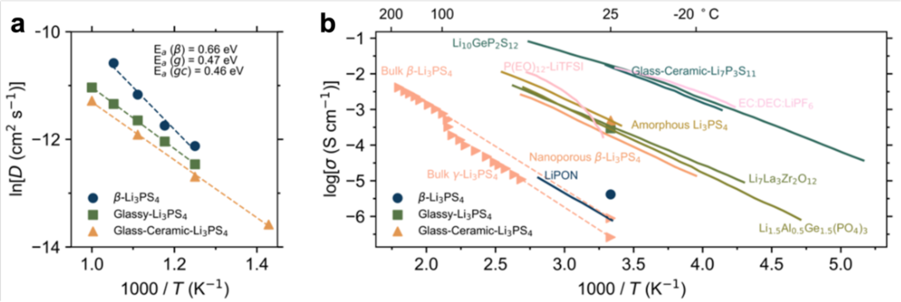

Figure 5-18 (a) Fit of Arrhenius type for the lithium diffusion coefficient's temperature dependency. (b) A comparison of the ionic conductivity's temperature dependency in $Li_3PS_4$ systems with different levels of disorder, together with findings for other lithium solid electrolytes, organic liquid electrolytes, and polymer electrolytes[82,84,108–115]. Figure reproduced from Paper V.

### 5.2.4. ION TRANSPORT WITHIN GLASS-CERAMIC STRUCTURES

From Figure 5-19a, we find that the glass phase and the interface perform better than the crystalline phase when we analyze the MSD data at 900 K. Figure 5-19b illustrates the heterogeneous dynamics using the NGP. As the degree of disorder increases, there is a corresponding rise in the NGP peak intensity. This shows that a larger divergence from Gaussian ion dynamics is associated with more disorder, in conjunction with the results shown in Figure 5-16a. Hoping ions exhibit a significant long-range movement over time at 900 K in the glassy (Figure 5-19c) and interfacial[98] regions of glass-ceramic $Li_3PS_4$. On the other hand, the crystalline phase does not exhibit the displacement distribution as observed in β-$Li_3PS_4$. Rather, it constantly displays a significant probability of displacements within the 3-10 Å range. This suggests that during thermal activation, lithium ions in the glass-ceramic's crystalline phase have a reduced ability to diffuse across the interface or migrate into the glass phase.

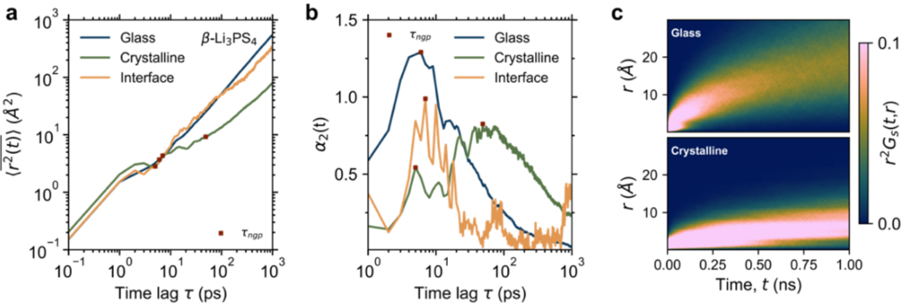

Figure 5-19 (a) MSD and (b) NGP of lithium of glass-ceramic $Li_3PS_4$ system. (c) Self-part van Hove correlation function for glass-ceramic $Li_3PS_4$ system. Figure reproduced from Paper V.

When compared to both glassy $Li_3PS_4$ and β-$Li_3PS_4$, the enhanced ionic conductivity observed in glass-ceramics is closely associated with the ion dynamics impacted by internal disorder in the glassy phase and the disordered interface. Glass-ceramic $Li_3PS_4$ samples regularly exhibit this enhancing effect (see Figure 5-20). Remarkably, the ionic conductivities of glass-ceramic $Li_3PS_4$ electrolytes, with different crystalline contents, at room temperature are more than two orders of magnitude greater than those of β-$Li_3PS_4$ and exceed those of the glassy $Li_3PS_4$ electrolyte.

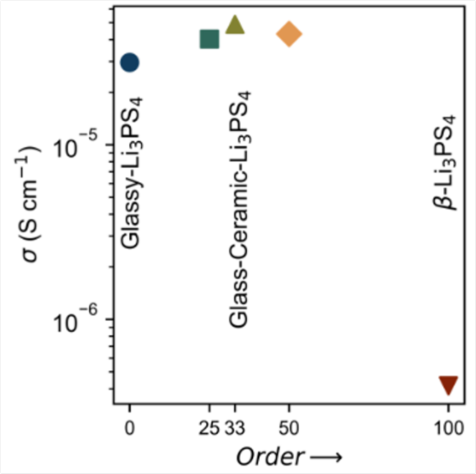

Figure 5-20 Ionic conductivities at 300 K of glassy, glass-ceramic $Li_3PS_4$, and β- $Li_3PS_4$ electrolytes. Figure reproduced from Paper V.

The migration pathways of a single lithium ion through the different phases of glass-ceramic are illustrated graphically in Figure 5-21. Ions follow meandering paths as they move across a complicated potential-energy environment in the glassy phase[59]. On the other hand, distinct site-to-site hopping pathways are present in the highly organized crystalline phase.

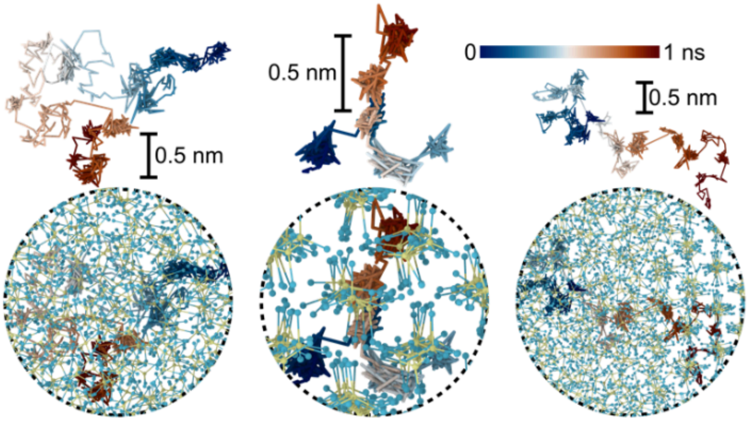

Figure 5-21 Atomic snapshots depict the migration trajectories of lithium ions in the glass (left), crystalline (middle), and interfacial (right) phases of the glass-ceramic electrolytes during a 1-ns time interval. Figure reproduced from Paper V.

This contrast underscores the significance of structural order in influencing ionic mobility. In disordered phases, the irregular potential landscape creates a complex migration environment, causing lithium ions to follow more tortuous paths. This can enhance ionic conductivity by providing multiple pathways and reducing the likelihood of bottlenecks. However, it also introduces variability in ionic motion, which can impact the overall efficiency and predictability of ion transport. In contrast, the ordered crystalline phase offers well-defined pathways, leading to more straightforward and predictable ion migration. These distinct site-to-site hopping mechanisms can facilitate rapid and efficient ionic movement but may also be more susceptible to disruptions if any defects or obstacles are present in the lattice structure. Understanding these dynamics is crucial for optimizing the performance of solid electrolytes in various applications.

# CHAPTER 6. CONCLUSIONS AND PERSPECTIVES

In this chapter, we will briefly summarize the main findings and their potential significance, as well as discuss perspectives and suggestions for future work.

## 6.1. CONCLUSIONS

Through this thesis, we have explored various factors influencing the mechanical properties and ion dynamics in disordered solid electrolytes, particularly focusing on lithium-containing glassy materials. Our research revealed significant insights into how structural modifications at both atomic and network levels impact the material properties, thereby guiding the design of high-performance glassy electrolytes and glasses with enhanced mechanical properties.

We have detailed the dependence of fracture toughness and ionic conductivity on the structural parameters of lithium borophosphate glassy electrolytes. The results underscored the importance of network openness and the coordination environment of lithium ions in achieving desirable material properties. Changes in the coordination numbers of boron in lithium borophosphate glassy electrolytes are strongly correlated with fracture toughness, and the propensity for changes in the coordination number of boron is also captured by a machine-learning algorithm called softness, which together explain the evidence that four-fold boron provides better ductility of lithium borophosphate glassy electrolytes. Meanwhile, we have also found that increasing the crystal content in LATP glass-ceramics enhances the fracture energy of the solid-state electrolyte.

By employing machine learning techniques, we have deciphered how different anion clusters in lithium thiophosphate glasses govern lithium conduction. The study highlighted the importance of polyatomic anion clusters in determining the mobility of lithium ions, providing a pathway to optimize electrolyte compositions for better performance. We have also showed that introducing disorder into solid-state electrolytes, such as through varying the local structural environments, can significantly enhance lithium-ion transport. This insight is crucial for the development of all-solid-state batteries with higher ionic conductivity and stability.

Collectively, these findings indicate that the structural design of solid electrolytes, at both micro and nano scales, plays a pivotal role in enhancing their mechanical and ion diffusion properties. Our research provides a robust framework for the rational design of next-generation disordered solid electrolytes with tailored properties for various applications.

## 6.2. PERSPECTIVES

While significant progress has been made in understanding the structural origins of fracture resistance and ionic conduction in glassy materials, several areas warrant further investigation to fully exploit these materials' potential.

1. Medium-Range Structural Changes: Future studies should delve deeper into the rearrangement of medium-range structures (MRO) and their impact on glassy electrolytes properties. Detailed investigations into how these MRO changes occur under different conditions, such as varying temperatures and stress environments, are essential. Additionally, the relationship between MRO and macroscopic properties like durability and thermal expansion should be elucidated. Advanced characterization techniques, such as neutron scattering and high-resolution transmission electron microscopy (HRTEM), could provide valuable insights into these mechanisms.

2. Fracture Toughness and Crack Growth: The behavior of crack growth and fracture toughness needs thorough exploration. In particular, the interaction between microstructural features, such as phase separations or inclusions, and crack propagation paths should be investigated. Research should also focus on the effects of incorporating second-phase particles or pretreated nanoparticles on the initiation and growth of cracks. Understanding these interactions at a microscopic level through techniques like *in-situ* mechanical testing and fracture surface analysis can offer insights into enhancing fracture toughness.

3. Advanced Computational Methods: The application of advanced computational methods, such as machine learning (ML) and molecular dynamics (MD) simulations, should be expanded to explore the vast compositional space of disordered electrolytes. ML algorithms can predict properties and identify promising compositions faster than traditional methods. Meanwhile, MD simulations can provide atomic-level insights into the behavior of glass under various conditions. Additionally, machine learning-based potential for MD simulations offer a powerful approach to accurately model atomic interactions in complex disordered systems. The potentials, trained on high-fidelity quantum mechanical calculations, can significantly enhance the efficiency and accuracy of simulations. Combining these methods with experimental validation can uncover new correlations and guide experimental efforts more effectively, thus accelerating the discovery of new disordered electrolytes with tailored properties.

4. Interfacial Phenomena: The role of interfaces in solid-state electrolytes and their impact on ionic conduction and mechanical stability is another critical area. Detailed studies on interface engineering, such as the development of interfacial coatings or the optimization of grain boundary chemistry, could lead to breakthroughs in the performance of all-solid-state batteries. Techniques like electrochemical impedance spectroscopy (EIS) and advanced microscopy methods should be utilized to

characterize these interfaces at high resolution and to understand their influence on ionic mobility and stability.

5. Ion hopping model: Ion hopping models applicable to disordered materials are still not fully established. Despite investigations into ion migration dynamics under disordered structures from various perspectives, a unified model for describing them is lacking. Future research should aim to develop comprehensive models that can accurately predict ion transport in these materials. This could involve integrating experimental data with theoretical frameworks to understand ion hopping mechanisms and their dependence on structural disorder. Techniques such as nuclear magnetic resonance (NMR) spectroscopy and computational modeling could play pivotal roles in these developments.

By addressing these research areas, we can further enhance the performance and applicability of disordered electrolytes or other disordered materials in various advanced technological applications, from energy storage to structural components. Such advancements will not only push the boundaries of current material science but also pave the way for the development of next-generation technologies that rely on the unique properties of disordered materials.

# BIOGRAPHY

[1] S. Chu, A. Majumdar, *Nature* **2012**, *488*, 294.

[2] X. Yang, X. Li, K. Adair, H. Zhang, X. Sun, *Electrochem. Energ. Rev.* **2018**, *1*, 239.

[3] Y.-J. Wang, B. Fang, D. Zhang, A. Li, D. P. Wilkinson, A. Ignaszak, L. Zhang, J. Zhang, *Electrochem. Energ. Rev.* **2018**, *1*, 1.

[4] J. Lu, Z. Chen, F. Pan, Y. Cui, K. Amine, *Electrochem. Energ. Rev.* **2018**, *1*, 35.

[5] B. Scrosati, J. Hassoun, Y.-K. Sun, *Energy Environ. Sci.* **2011**, *4*, 3287.

[6] H. Liu, X.-B. Cheng, J.-Q. Huang, H. Yuan, Y. Lu, C. Yan, G.-L. Zhu, R. Xu, C.-Z. Zhao, L.-P. Hou, C. He, S. Kaskel, Q. Zhang, *ACS Energy Lett.* **2020**, *5*, 833.

[7] M. Armand, J.-M. Tarascon, *Nature* **2008**, *451*, 652.

[8] J. A. Dawson, P. Canepa, T. Famprikis, C. Masquelier, M. S. Islam, *J. Am. Chem. Soc.* **2018**, *140*, 362.

[9] J. Janek, W. G. Zeier, *Nat Energy* **2016**, *1*, 16141.

[10] J. B. Goodenough, K.-S. Park, *J. Am. Chem. Soc.* **2013**, *135*, 1167.

[11] J. B. Goodenough, Y. Kim, *Chem. Mater.* **2010**, *22*, 587.

[12] Z. Zhang, Y. Shao, B. Lotsch, Y.-S. Hu, H. Li, J. Janek, L. F. Nazar, C.-W. Nan, J. Maier, M. Armand, L. Chen, *Energy Environ. Sci.* **2018**, *11*, 1945.

[13] L. Porz, T. Swamy, B. W. Sheldon, D. Rettenwander, T. Frömling, H. L. Thaman, S. Berendts, R. Uecker, W. C. Carter, Y.-M. Chiang, *Advanced Energy Materials* **2017**, *7*, 1701003.

[14] R. Koerver, W. Zhang, L. de Biasi, S. Schweidler, A. O. Kondrakov, S. Kolling, T. Brezesinski, P. Hartmann, W. G. Zeier, J. Janek, *Energy Environ. Sci.* **2018**, *11*, 2142.

[15] T. Famprikis, P. Canepa, J. A. Dawson, M. S. Islam, C. Masquelier, *Nat. Mater.* **2019**, *18*, 1278.

[16] V. Viallet, V. Seznec, A. Hayashi, M. Tatsumisago, A. Pradel, In *Springer Handbook of Glass* (Eds.: Musgraves, J. D.; Hu, J.; Calvez, L.), Springer International Publishing, Cham, **2019**, pp. 1697–1754.

[17] K. E. Aifantis, J. P. Dempsey, *Journal of Power Sources* **2005**, *143*, 203.

[18] C. E. Athanasiou, X. Liu, M. Y. Jin, E. Nimon, S. Visco, C. Lee, M. Park, J. Yun, N. P. Padture, H. Gao, B. W. Sheldon, *Cell Reports Physical Science* **2022**, *3*, 100845.

[19] A. Chandra, A. Bhatt, A. Chandra, *Journal of Materials Science & Technology* **2013**, *29*, 193.

[20] A. Bunde, K. Funke, M. D. Ingram, *Solid State Ionics* **1998**, *105*, 1.

[21] W. H. Zachariasen, *J. Am. Chem. Soc.* **1932**, *54*, 3841.

[22] P. Y. Huang, S. Kurasch, A. Srivastava, V. Skakalova, J. Kotakoski, A. V. Krasheninnikov, R. Hovden, Q. Mao, J. C. Meyer, J. Smet, D. A. Muller, U. Kaiser, *Nano Lett.* **2012**, *12*, 1081.

[23] K. A. Kirchner, D. R. Cassar, E. D. Zanotto, M. Ono, S. H. Kim, K. Doss, M. L. Bødker, M. M. Smedskjaer, S. Kohara, L. Tang, M. Bauchy, C. J. Wilkinson, Y. Yang, R. S. Welch, M. Mancini, J. C. Mauro, *Chem. Rev.* **2022**.

[24] Y. Yang, J. Zhou, F. Zhu, Y. Yuan, D. J. Chang, D. S. Kim, M. Pham, A. Rana, X. Tian, Y. Yao, S. J. Osher, A. K. Schmid, L. Hu, P. Ercius, J. Miao, *Nature* **2021**, *592*, 60.
[25] S. R. Elliott, *J. Phys.: Condens. Matter* **1992**, *4*, 7661.
[26] S. R. Elliott, *Phys. Rev. Lett.* **1991**, *67*, 711.
[27] C. Kittel, P. McEuen, *Introduction to Solid State Physics*, John Wiley & Sons, **2018**.
[28] B. E. Warren, *Phys. Rev.* **1934**, *45*, 657.
[29] A. Soper, *Rutherford Appleton Laboratory Technical Reports* **2011**.
[30] D. A. Keen, *J Appl Crystallogr* **2001**, *34*, 172.
[31] Q. Zhou, Y. Shi, B. Deng, J. Neuefeind, M. Bauchy, *Science Advances* **2021**, *7*, eabh1761.
[32] V. Lacivita, A. S. Westover, A. Kercher, N. D. Phillip, G. Yang, G. Veith, G. Ceder, N. J. Dudney, *J. Am. Chem. Soc.* **2018**, *140*, 11029.
[33] X. Liu, J. Zhou, S. Zhou, Y. Yue, J. Qiu, *Progress in Materials Science* **2018**, *97*, 38.
[34] C. Dietrich, D. A. Weber, S. J. Sedlmaier, S. Indris, S. P. Culver, D. Walter, J. Janek, W. G. Zeier, *J. Mater. Chem. A* **2017**, *5*, 18111.
[35] Y. Lee, Y.-H. Kim, J.-H. An, J.-C. Lee, *Acta Materialia* **2022**, *235*, 118106.
[36] K. Ohara, A. Mitsui, M. Mori, Y. Onodera, S. Shiotani, Y. Koyama, Y. Orikasa, M. Murakami, K. Shimoda, K. Mori, T. Fukunaga, H. Arai, Y. Uchimoto, Z. Ogumi, *Sci Rep* **2016**, *6*, 21302.
[37] C. Dietrich, M. Sadowski, S. Sicolo, D. A. Weber, S. J. Sedlmaier, K. S. Weldert, S. Indris, K. Albe, J. Janek, W. G. Zeier, *Chem. Mater.* **2016**, *28*, 8764.
[38] S. Plimpton, *Journal of Computational Physics* **1995**, *117*, 1.
[39] O. T. Unke, S. Chmiela, H. E. Sauceda, M. Gastegger, I. Poltavsky, K. T. Schütt, A. Tkatchenko, K.-R. Müller, *Chem. Rev.* **2021**, *121*, 10142.
[40] P. Hohenberg, W. Kohn, *Phys. Rev.* **1964**, *136*, B864.
[41] W. Kohn, L. J. Sham, *Phys. Rev.* **1965**, *140*, A1133.
[42] C. Lee, W. Yang, R. G. Parr, *Phys. Rev. B* **1988**, *37*, 785.
[43] J. P. Perdew, Y. Wang, *Phys. Rev. B* **1992**, *45*, 13244.
[44] J. C. Slater, *Phys. Rev.* **1951**, *81*, 385.
[45] R. A. Buckingham, J. E. Lennard-Jones, *Proceedings of the Royal Society of London. Series A. Mathematical and Physical Sciences* **1997**, *168*, 264.
[46] S. Stegmaier, R. Schierholz, I. Povstugar, J. Barthel, S. P. Rittmeyer, S. Yu, S. Wengert, S. Rostami, H. Kungl, K. Reuter, R. Eichel, C. Scheurer, *Adv. Energy Mater.* **2021**, *11*, 2100707.
[47] J. D. Musgraves, J. Hu, L. Calvez, Eds., *Springer Handbook of Glass*, Springer International Publishing, Cham, **2019**.
[48] P. A. M. Dirac, R. H. Fowler, *Proceedings of the Royal Society of London. Series A, Containing Papers of a Mathematical and Physical Character* **1997**, *123*, 714.
[49] Y. Gao, B. Zhang, *Advanced Materials* **2023**, *35*, 2205421.
[50] F. P. McGrogan, T. Swamy, S. R. Bishop, E. Eggleton, L. Porz, X. Chen, Y. Chiang, K. J. Van Vliet, *Adv. Energy Mater.* **2017**, *7*, 1602011.

[51] J. Li, J. Cho, J. Ding, H. Charalambous, S. Xue, H. Wang, X. L. Phuah, J. Jian, X. Wang, C. Ophus, T. Tsakalakos, R. E. García, A. K. Mukherjee, N. Bernstein, C. S. Hellberg, H. Wang, X. Zhang, *Science Advances* **2019**, *5*, eaaw5519.

[52] L. Porz, A. J. Klomp, X. Fang, N. Li, C. Yildirim, C. Detlefs, E. Bruder, M. Höfling, W. Rheinheimer, E. A. Patterson, P. Gao, K. Durst, A. Nakamura, K. Albe, H. Simons, J. Rödel, *Materials Horizons* **2021**, *8*, 1528.

[53] S. Kalnaus, N. J. Dudney, A. S. Westover, E. Herbert, S. Hackney, *Science* **2023**, *381*, eabg5998.

[54] S. Kalnaus, A. S. Westover, M. Kornbluth, E. Herbert, N. J. Dudney, *Journal of Materials Research* **2021**, *36*, 787.

[55] B. Lawn, *Fracture of Brittle Solids*, 2nd ed., Cambridge University Press, Cambridge, **1993**.

[56] J. E. Srawley, *Int J Fract* **1976**, *12*, 475.

[57] T. To, F. Célarié, C. Roux-Langlois, A. Bazin, Y. Gueguen, H. Orain, M. Le Fur, V. Burgaud, T. Rouxel, *Acta Materialia* **2018**, *146*, 1.

[58] H. Niu, S. Niu, A. R. Oganov, *Journal of Applied Physics* **2019**, *125*, 065105.

[59] J. C. Dyre, P. Maass, B. Roling, D. L. Sidebottom, *Rep. Prog. Phys.* **2009**, *72*, 046501.

[60] Z. Zhu, I.-H. Chu, Z. Deng, S. P. Ong, *Chem. Mater.* **2015**, *27*, 8318.

[61] N. J. J. de Klerk, M. Wagemaker, *Chem. Mater.* **2016**, *28*, 3122.

[62] K. Mori, T. Kasai, K. Iwase, F. Fujisaki, Y. Onodera, T. Fukunaga, *Solid State Ionics* **2017**, *301*, 163.

[63] S. Adams, J. Swenson, *J. Phys.: Condens. Matter* **2005**, *17*, S87.

[64] Z. Chen, T. Du, S. S. Sørensen, R. Christensen, Q. Zhang, L. R. Jensen, O. V. Magdysyuk, M. Diaz-Lopez, M. Bauchy, Y. Yue, M. M. Smedskjaer, *Journal of Power Sources* **2023**, *553*, 232302.

[65] A. C. Wright, *Journal of Non-Crystalline Solids* **1993**, *159*, 264.

[66] C. Hermansen, R. E. Youngman, J. Wang, Y. Yue, *J. Chem. Phys.* **2015**, *142*, 184503.

[67] Y. Kato, H. Yamazaki, S. Yoshida, J. Matsuoka, *Journal of Non-Crystalline Solids* **2010**, *356*, 1768.

[68] T. To, L. R. Jensen, M. M. Smedskjaer, *Journal of Non-Crystalline Solids* **2020**, *534*, 119946.

[69] E. J. Frankberg, J. Kalikka, F. García Ferré, L. Joly-Pottuz, T. Salminen, J. Hintikka, M. Hokka, S. Koneti, T. Douillard, B. Le Saint, P. Kreiml, M. J. Cordill, T. Epicier, D. Stauffer, M. Vanazzi, L. Roiban, J. Akola, F. Di Fonzo, E. Levänen, K. Masenelli-Varlot, *Science* **2019**, *366*, 864.

[70] T. To, S. S. Sørensen, J. F. S. Christensen, R. Christensen, L. R. Jensen, M. Bockowski, M. Bauchy, M. M. Smedskjaer, *ACS Appl. Mater. Interfaces* **2021**, *13*, 17753.

[71] T. Du, H. Liu, L. Tang, S. S. Sørensen, M. Bauchy, M. M. Smedskjaer, *ACS Nano* **2021**, *15*, 17705.

[72] S. S. Schoenholz, E. D. Cubuk, D. M. Sussman, E. Kaxiras, A. J. Liu, *Nature Phys* **2016**, *12*, 469.

[73] E. D. Cubuk, R. J. S. Ivancic, S. S. Schoenholz, D. J. Strickland, A. Basu, Z. S. Davidson, J. Fontaine, J. L. Hor, Y.-R. Huang, Y. Jiang, N. C. Keim, K. D.

Koshigan, J. A. Lefever, T. Liu, X.-G. Ma, D. J. Magagnosc, E. Morrow, C. P. Ortiz, J. M. Rieser, A. Shavit, T. Still, Y. Xu, Y. Zhang, K. N. Nordstrom, P. E. Arratia, R. W. Carpick, D. J. Durian, Z. Fakhraai, D. J. Jerolmack, D. Lee, J. Li, R. Riggleman, K. T. Turner, A. G. Yodh, D. S. Gianola, A. J. Liu, *Science* **2017**, *358*, 1033.

[74] H. Liu, S. Xiao, L. Tang, E. Bao, E. Li, C. Yang, Z. Zhao, G. Sant, M. M. Smedskjaer, L. Guo, M. Bauchy, *Acta Materialia* **2021**, *210*, 116817.

[75] Q. Wang, L. Zhang, *Nat Commun* **2021**, *12*, 5359.

[76] Z. Fan, E. Ma, *Nat Commun* **2021**, *12*, 1506.

[77] E. D. Cubuk, S. S. Schoenholz, J. M. Rieser, B. D. Malone, J. Rottler, D. J. Durian, E. Kaxiras, A. J. Liu, *Phys. Rev. Lett.* **2015**, *114*, 108001.

[78] T. Du, Z. Chen, H. Liu, Q. Zhang, M. Bauchy, Y. Yue, M. M. Smedskjaer, *Materials Today Energy* **2023**, *37*, 101390.

[79] Z. Chen, T. Du, N. M. A. Krishnan, M. M. Smedskjaer, *J. Mater. Chem. A* **2024**, *12*, 3061.

[80] Z. Deng, Z. Wang, I.-H. Chu, J. Luo, S. P. Ong, *J. Electrochem. Soc.* **2015**, *163*, A67.

[81] G. Yan, S. Yu, W. Yang, X. Li, H. Tempel, H. Kungl, R.-A. Eichel, M. Krüger, J. Malzbender, *Journal of Power Sources* **2019**, *437*, 226940.

[82] Z. Liu, W. Fu, E. A. Payzant, X. Yu, Z. Wu, N. J. Dudney, J. Kiggans, K. Hong, A. J. Rondinone, C. Liang, *J. Am. Chem. Soc.* **2013**, *135*, 975.

[83] F. Mizuno, A. Hayashi, K. Tadanaga, M. Tatsumisago, *Advanced Materials* **2005**, *17*, 918.

[84] Y. Seino, T. Ota, K. Takada, A. Hayashi, M. Tatsumisago, *Energy Environ. Sci.* **2014**, *7*, 627.

[85] K. Uchida, T. Ohkubo, F. Utsuno, K. Yazawa, *ACS Appl. Mater. Interfaces* **2021**, *13*, 37071.

[86] M. B. Preefer, J. H. Grebenkemper, C. E. Wilson, M. Everingham, J. A. Cooley, R. Seshadri, *ACS Appl. Mater. Interfaces* **2021**, *13*, 57567.

[87] S. Ariga, T. Ohkubo, S. Urata, Y. Imamura, T. Taniguchi, *Phys. Chem. Chem. Phys.* **2022**, *24*, 2567.

[88] Z. Chen, T. Du, R. Christensen, M. Bauchy, M. M. Smedskjaer, *ACS Energy Lett.* **2023**, 1969.

[89] J. G. Smith, D. J. Siegel, *Nat Commun* **2020**, *11*, 1483.

[90] M. Sadowski, K. Albe, *Journal of Power Sources* **2020**, *478*, 229041.

[91] K. Mori, K. Enjuji, S. Murata, K. Shibata, Y. Kawakita, M. Yonemura, Y. Onodera, T. Fukunaga, *Phys. Rev. Applied* **2015**, *4*, 054008.

[92] K. Mori, T. Ichida, K. Iwase, T. Otomo, S. Kohara, H. Arai, Y. Uchimoto, Z. Ogumi, Y. Onodera, T. Fukunaga, *Chemical Physics Letters* **2013**, *584*, 113.

[93] I.-H. Chu, H. Nguyen, S. Hy, Y.-C. Lin, Z. Wang, Z. Xu, Z. Deng, Y. S. Meng, S. P. Ong, *ACS Appl. Mater. Interfaces* **2016**, *8*, 7843.

[94] H. Liu, M. M. Smedskjaer, M. Bauchy, *Phys. Rev. B* **2022**, *106*, 214206.

[95] X. He, Y. Zhu, Y. Mo, *Nat Commun* **2017**, *8*, 15893.

[96] J.-S. Kim, W. D. Jung, J.-W. Son, J.-H. Lee, B.-K. Kim, K.-Y. Chung, H.-G. Jung, H. Kim, *ACS Appl. Mater. Interfaces* **2019**, *11*, 13.

[97] H. Wang, L. Zhang, J. Han, W. E, *Computer Physics Communications* **2018**, *228*, 178.
[98] Z. Chen, T. Du, N. M. A. Krishnan, Y. Yue, M. M. Smedskjaer, *Disorder-induced enhancement of lithium-ion transport in solid-state electrolytes*, arXiv, **2024**.
[99] K. Kaup, L. Zhou, A. Huq, L. F. Nazar, *J. Mater. Chem. A* **2020**, *8*, 12446.
[100] A. D. Poletayev, J. A. Dawson, M. S. Islam, A. M. Lindenberg, *Nat. Mater.* **2022**, *21*, 1066.
[101] S. Song, S. J. Park, M. Kim, J. S. Kim, B. J. Sung, S. Lee, J.-H. Kim, J. Sung, *Proceedings of the National Academy of Sciences* **2019**, *116*, 12733.
[102] F. N. Forrester, J. A. Quirk, T. Famprikis, J. A. Dawson, *Chem. Mater.* **2022**, *34*, 10561.
[103] A. Hayashi, S. Hama, T. Minami, M. Tatsumisago, *Electrochemistry Communications* **2003**, *5*, 111.
[104] H. Tsukasaki, S. Mori, S. Shiotani, H. Yamamura, *Solid State Ionics* **2018**, *317*, 122.
[105] F. Mizuno, A. Hayashi, K. Tadanaga, M. Tatsumisago, *Solid State Ionics* **2006**, *177*, 2721.
[106] M. Eom, J. Kim, S. Noh, D. Shin, *Journal of Power Sources* **2015**, *284*, 44.
[107] M. Tatsumisago, S. Hama, A. Hayashi, H. Morimoto, T. Minami, *Solid State Ionics* **2002**, *154–155*, 635.
[108] P. Mirmira, J. Zheng, P. Ma, C. V. Amanchukwu, *J. Mater. Chem. A* **2021**, *9*, 19637.
[109] M. Tachez, J.-P. Malugani, R. Mercier, G. Robert, *Solid State Ionics* **1984**, *14*, 181.
[110] X. Yu, J. B. Bates, G. E. Jellison, F. X. Hart, *J. Electrochem. Soc.* **1997**, *144*, 524.
[111] N. Kamaya, K. Homma, Y. Yamakawa, M. Hirayama, R. Kanno, M. Yonemura, T. Kamiyama, Y. Kato, S. Hama, K. Kawamoto, A. Mitsui, *Nature Mater* **2011**, *10*, 682.
[112] H. Buschmann, J. Dölle, S. Berendts, A. Kuhn, P. Bottke, M. Wilkening, P. Heitjans, A. Senyshyn, H. Ehrenberg, A. Lotnyk, V. Duppel, L. Kienle, J. Janek, *Physical Chemistry Chemical Physics* **2011**, *13*, 19378.
[113] B. E. Francisco, C. R. Stoldt, J.-C. M'Peko, *Chem. Mater.* **2014**, *26*, 4741.
[114] L. Edman, A. Ferry, M. M. Doeff, *Journal of Materials Research* **2000**, *15*, 1950.
[115] P. E. Stallworth, J. J. Fontanella, M. C. Wintersgill, C. D. Scheidler, J. J. Immel, S. G. Greenbaum, A. S. Gozdz, *Journal of Power Sources* **1999**, *81–82*, 739.

# LIST OF PUBLICATIONS

## PUBLICATIONS IN PEER-REVIEW JOURNALS

*Contributed as first author or main co-author:*

**Chen, Z.**, Du, T., Krishnan, N. M. A., Yue, Y. Z., Smedskjaer M. M (2024). Disorder-induced enhancement of lithium-ion transport in solid-state electrolytes. arXiv preprint, 2401.05151.

**Chen, Z.**, Du, T., Krishnan, N. A., & Smedskjaer, M. M. (2024). Enhanced bond switching at complexion layer facilitates high fracture energy of LATP solid-state electrolytes. *Journal of Materials Chemistry A*, 12(5), 3061-3071.

Du, T., **Chen, Z.**, Liu, H., Zhang, Q., Bauchy, M., Yue, Y., & Smedskjaer, M. M. (2023). Controlling factor for fracture resistance and ionic conduction in glassy lithium borophosphate electrolytes. *Materials Today Energy*, 37, 101390.

**Chen, Z.**, Du, T., Christensen, R., Bauchy, M., & Smedskjaer, M. M. (2023). Deciphering how anion clusters govern lithium conduction in glassy thiophosphate electrolytes through machine learning. *ACS Energy Letters*, 8(4), 1969-1975.

**Chen, Z.**, Du, T., Sørensen, S. S., Christensen, R., Zhang, Q., Jensen, L. R., ... & Smedskjaer, M. M. (2023). Structure dependence of fracture toughness and ionic conductivity in lithium borophosphate glassy electrolytes for all- solid-state batteries. *Journal of Power Sources*, 553, 232302.

*Contributed as co-author:*

Xiao, Y., Du, T., Sørensen, S. S., **Chen, Z.**, Biscio, C. A., Fajstrup, L., ... & Smedskjaer, M. M. (2023). Deciphering the hierarchical structure of phosphate glasses using persistent homology with optimized input radii. Physical Review Materials, 7(6), 065602.

## ORAL AND POSTER PRESENTATIONS AT CONFERENCES

**Chen, Z.,** Tao Du, N. M. Anoop Krishnan, Smedskjær, M. M. (2024) Fracture behavior of LATP glass-ceramic electrolytes: A molecular dynamics study. *2024 Glass & Optical Materials Division Annual Meeting*. Las Vegas, United States, Nevada.

**Chen, Z.,** Du T., Christensen, R., Bauchy, M., Smedskjær, M. M. (2024) Analyzing lithium-ion conduction in thiophosphate glassy electrolytes via machine learning. *2024 Glass & Optical Materials Division Annual Meeting*. Las Vegas, United States, Nevada.

**Chen, Z.**, Du, T., Sørensen, S. S., Christensen, R., Zhang, Q., Jensen, L. R., ... & Smedskjær, M. M. (2022). Atomistic origin of variation in toughness and ionic conductivity in lithium borophosphate glassy electrolytes. I*n The International Year of Glass Symposium 2022*, Aalborg, Denmark,

**Chen, Z.**, Du, T., Christensen, R., Bauchy, M., & Smedskjær, M. M. (2023). Analyzing lithium ion conductivity in thiophosphate glassy electrolytes via machine learning. In *Electrochemical Science and Technology Conference 2023*. Aalborg, Denmark.